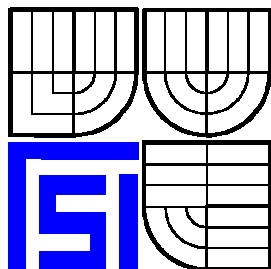# VYSOKÉ UČENÍ TECHNICKÉ V BRNĚ
BRNO UNIVERSITY OF TECHNOLOGY

FAKULTA STROJNÍHO INŽENÝRSTVÍ
ÚSTAV FYZIKÁLNÍHO INŽENÝRSTVÍ

FACULTY OF MECHANICAL ENGINEERING
INSTITUTE OF PHYSICAL ENGINEERING

HELIOVÝ KRYOSTAT PRO STUDIUM TURBULENTNÍHO PROUDĚNÍ PŘI PŘIROZENÉ KONVEKCI

HELIUM CRYOSTAT FOR EXPERIMENTAL STUDY OF NATURAL TURBULENT CONVECTION

DISERTAČNÍ PRÁCE

DOCTORAL THESIS

AUTOR PRÁCE   **Ing. PAVEL URBAN**
AUTHOR

VEDOUCÍ PRÁCE   **RNDr. VĚRA MUSILOVÁ, CSc.**
SUPERVISOR

ŠKOLITEL SPECIALISTA   **prof. RNDr. LADISLAV SKRBEK, DrSc.**
SUPERVISOR SPECIALIST

BRNO 2009

This doctoral thesis was elaborated at the

Institute of Scientific Instruments of the AS CR, v. v. i.

accredited for the doctoral study programme
„Physical and Materials Engineering"
decision of the MŠMT on 12st. February. 2008

under supervision of:
RNDr. Věra Musilová, CSc.

Abstrakt

V disertační práci je popsán heliový kryostat s experimentální válcovou konvekční celou pro studium proudění při přirozené konvekci za velmi vysokých Rayleigho čísel Ra (až do řádu 10^{15}) a Nusseltových čísel Nu (až do řádu 10^4). Pracovní látkou je studené ^{4}He, které umožňuje díky výhodným fyzikálním vlastnostem dosažení velmi vysokých hodnot čísel Ra. Návrh kryostatu je založen na koncepci lázňových NMR kryostatů s nízkým odparem kryokapalin. Ve středu kryostatu je umístěna konvekční cela o průměru 300 mm a výšce 300 mm. Celu tvoří horní a spodní dno a výměnná střední část. Tyto díly jsou spojeny rozebíratelnými přírubami těsněnými indiovým drátem. Výměnná část umožňuje snadnou modifikaci geometrie cely. Hlavní přednost kryostatu spočívá v minimálním vlivu konstrukce cely a použitých materiálů na studovanou konvekci. Cela kryostatu je navržena pro pracovní tlaky do 250 kPa.

Abstract

The thesis focuses on the design of a helium cryostat with an experimental convection cell for the study of natural turbulent convection in the range of Rayleigh numbers Ra up to 10^{15} and Nusselt numbers Nu up to 10^4. Cryogenic ^{4}He gas is used as a working fluid for experimental studies due to its advantageous properties that allow reaching very high Ra numbers. The cryostat design is based on the conception of low-loss NMR magnet cryostats. In the centre of the cryostat a cylindrical convection cell of 300 mm in diameter and 300 mm in height is placed. The cell is made of middle, top and bottom parts. These are jointed together by flanges sealed by indium wires. The middle part is exchangeable and allows the geometry of the cell to be modified. The cell is designed for measurements at pressures up to 250 kPa. The main advantage of this cryostat is the minimal influence of the cell design and materials on the studied convection.

Keywords

helium cryostat, turbulent flow, natural convection, Rayleigh-Bénard convection, heat transfer, Rayleigh number

Klíčová slova

heliový kryostat, turbulentní proudění, přirozená konvekce, Rayleigh-Bénardova konvekce, přenos tepla, Rayleighovo číslo

Bibliografická citace

Urban, P. *Heliový kryostat pro studium turbulentního proudění při přirozené konvekci*. 2009, Brno : Vysoké učení technické v Brně, Fakulta strojního inženýrství, 2009. 67 s. Vedoucí disertační práce RNDr. Věra Musilová, CSc.

Affirmation

I declare that my thesis "Helium Cryostat for Experimental Study of Natural Turbulent Convection" was elaborated by myself under professional leadership by my supervisor.

Signature:

Prohlášení autora o původnosti práce

Prohlašuji, že jsem disertační práci na téma „Heliový kryostat pro studium turbulentního proudění při přirozené konvekci" vypracoval samostatně pod vedením RNDr. Věry Musilové, CSc.

Podpis:

Acknowledgements

I would like to express my gratitude and thanks to all colleagues from the Institute of Scientific Instruments, v.v.i. who co-operated on the development and realization of the apparatus which is described in this thesis:

Development of the apparatus
Pavel Hanzelka, Josef Jelínek, Jiří Kališ, Věra Musilová, Aleš Srnka
Vacuum brazing and electron beam welding
Jan Dupák, Libor Dupák, Petr Kapounek, Eduard Kunc
Measurement of the Ni layers thickness, material and metallographic analysis
Jaroslav Sobota, Tomáš Fořt, Miloslav Ledvina, Jiří Runštuk
Manufacture of the cryostat parts
members of the workshop
Technical background of Group of Cryogenic and Superconductivity
Václav Dalecký, Vladimír Heinige, Zdeněk Krejčí

I would like to express my special thanks to my supervisor Dr. V. Musilová and Dr. L. Skrbek, for their guidance and stimulating discussions throughout the project. I thank to Dr. L. Skrbek for his idea to start the investigations of turbulent convection.

Poděkování

Na tomto místě bych rád vyjádřil poděkování pracovníkům z Ústavu přístrojové techniky AV ČR, v.v.i., kteří se podíleli na vývoji a realizaci aparatury popisované v této disertační práci:

Vývoj aparatury
Pavel Hanzelka, Jiří Kališ, Josef Jelínek, Věra Musilová, Aleš Srnka
Vakuové pájení a svařování elektronovým svazkem
Jan Dupák, Libor Dupák, Petr Kapounek, Eduard Kunc
Měření tloušťek Ni vrstev, metalografické vzorky, materiálová analýza
Jaroslav Sobota, Tomáš Fořt, Miloslav Ledvina, Jiří Runštuk
Výroba součástí kryostatu
pracovníci dílen
Technické zázemí Skupiny kryogeniky a supravodivosti
Václav Dalecký, Vladimír Heinige, Zdeněk Krejčí

Zvláště děkuji mé vedoucí disertační práce RNDr. Věře Musilové, CSc. a prof. RNDr. Ladislavu Skrbkovi, DrSc. za metodické vedení, podnětné diskuze a podporu během studia.

Contents

1 The state-of-art

1.1 Introduction

Turbulent natural convection plays a prominent role in heat transport phenomena such as atmospheric and oceanic circulation, geodynamics, stellar convection and relevant industrial applications.

As a fundamental theory based on first principles is absent, dimensionless numbers and phenomenological analyses are generally used to describe fluid flows. The most relevant issue is then to estimate the corresponding scaling laws. Without their knowledge, scaling-up from laboratory models to actual processes is not possible. Many researchers are consequently performing experiments and computations worldwide to gain a better understanding of turbulent convection and are engaged in lively discussions on controversial outcomes.

The simplest configuration of natural convection is known as the Rayleigh-Bénard convection (RBC). It is defined as a thermally driven flow in a fluid layer between two infinite rigid horizontal plates, where constant temperatures are imposed on both fluid boundaries (Figure 1) [1]. The bottom plate is heated and the top one is cooled. The warmer fluid at the bottom expands and produces an unstable density gradient in the fluid layer (in gravitational field). If the density gradient is sufficiently strong, the hot fluid will rise up and onset a convective flow which results in an enhanced transport of heat between the two plates. The basic issue is to find a relation between the heat flux density H transferred by convection and the temperature difference ΔT between the bottom and top plates.
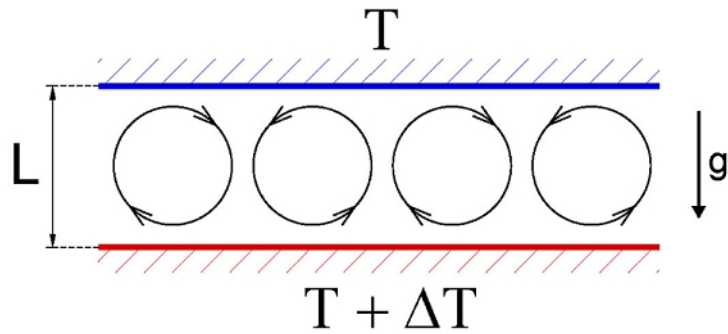
Figure 1   Schematic representation of the Rayleigh-Bénard convection

The convection heat transfer can be characterised by the Nusselt number *Nu*

$$Nu = \frac{H}{H_0} = \frac{L \cdot H}{\lambda \cdot \Delta T}, \tag{1}$$

representing a dimensionless ratio of the measured density of the heat flux H to the conductive density of the heat flux $H_0 = \lambda \cdot \Delta T / L$, that would occur in the fluid without motion. Here λ is the heat conductivity of the fluid and L is the height of the fluid layer.

From the dimensional analysis of the mass, momentum and energy conservation equations of an almost incompressible fluid (Boussinesq approximation), it follows that the description of the RBC depends on two dimensionless parameters. These are the Rayleigh number *Ra*,

$$Ra = \frac{g \cdot \alpha \cdot \Delta T \cdot L^3}{\nu \cdot \kappa} \qquad (2)$$

and Prandtl number Pr,

$$Pr = \frac{\nu}{\kappa}, \qquad (3)$$

where g is the gravity acceleration, α, ν and κ are the isobaric thermal expansion coefficient, kinematic viscosity and thermal diffusivity, respectively. The onset of the RBC between infinite plates is theoretically predicted for the critical Rayleigh number $Ra_c = 1708$ which agrees with its experimental value. A possible convection pattern shortly after onset of the convective flow is shown in Figure 1.

The Boussinesq condition

$$\alpha \cdot \Delta T << 1 \qquad (4)$$

justifies the assumption of "incompressibility" of the working fluid in experiments with gaseous fluids [1]. Variations of the density are only a source of buoyancy force in this approximation.

1.2 Scaling laws of natural convection

1.2.1 $Nu(Ra)$ dependence

The Rayleigh-Bénard convection is a model for fundamental convection studies [1]. The fluid layer becomes turbulent typically at Rayleigh numbers Ra exceeding 10^5, except for the boundary layer. In experiments on the RBC in turbulent regime a power law is obtained, that is

$$Nu \sim Ra^\gamma, \qquad (5)$$

where γ is usually close to 1/3.

The power law with γ close to 1/3 corresponds to a simplified model of convection, where all the temperature difference ΔT drops on the boundary layers (thin in comparison with L) while the central turbulent fluid is effectively mixed and has a nearly constant temperature. Heat transfer is thus controlled by heat conduction of the boundary layers and convective heat flux does not consequently depend on the height L of the fluid. This fact explicates the $\gamma = 1/3$ power law.

1.2.2 Kraichnan regime

Turbulence effects start to be independent on the fluid viscosity when the fluid velocity is sufficiently large, i.e. when viscous damping is negligible in comparison with flow inertia. In natural convection this assumption results in the relation

$$Nu \sim Ra^{1/2} \qquad (6)$$

for high Ra (for high driving buoyancy force) [2].

This regime is called the "ultimate regime" or "Kraichnan regime" and was first predicted by Kraichnan [3] for high values of Ra. For values $0.15 < Pr < 1$, he stated that

$$Nu \sim Ra^{1/2} \, Pr^{-1/4} \qquad (7)$$

with a $(\log Ra)^{(-3/2)}$ correction [3].

The boundary layer should undergo a laminar-turbulent transition for high Ra numbers and the heat flux is not anymore controlled by the laminar boundary layers in this regime.

Many large thermal circulations on the Earth, such as the atmospheric one, occur at high values of *Ra*, and are not easy or even impossible to be modelled in laboratory conditions. Unfortunately, discrepancies among experiments, results of numerical simulations, predictions on *Nu*(*Ra, Pr*) dependence and onset of Kraichnan regime reveal a general lack of understanding. Experimental evidence of the predicted Kraichnan regime is thus of fundamental interest. In spite of considerable efforts, a convincing experiment that has unequivocally solved this question has yet to be performed [4], [5].

It is difficult to predict the *Ra* value at which an ultimate regime sets on. Kraichnan supposed an onset at extremely high values which have not yet been achieved in any laboratory. On the other hand, Kraichnan regime $Nu \sim Ra^{1/2}$ was observed in numerically simulated natural convection in a fluid with $Pr = 1$ at $Ra = 10^6 - 10^7$ [6], where the bulk fluid was simulated, without the boundary layer, by imposing periodic boundary conditions on the fluid.

1.3 Experiments

1.3.1 Laboratory model of RBC

In laboratory conditions the RBC may be studied in a cylindrical cell with negligibly thermally conductive sidewalls, closed on its top and bottom sides by high heat conductivity and capacity plates. The geometry of the cell is characterized by the aspect ratio $\Gamma = D/L$, where *L* is the distance between the plates and *D* the inner diameter of the cell.

As mentioned above, the heat transferred by natural convection is given by a scaling relation $Nu = f(Ra, Pr)$ which in general depends also on the aspect ratio Γ.

1.3.2 Large scale circulation

For the overall understanding of turbulent convection, it is also significant to know the behaviour of the fluid inside the cell. Organized flow structures inside the cell, such as large-scale circulation, plumes and jets, are observed in experiments [7], [8] and numerical simulations [9], [4]. The large scale circulation, called "wind" [10], has a dimension of the order of the size of the convection cell (Figure 2).

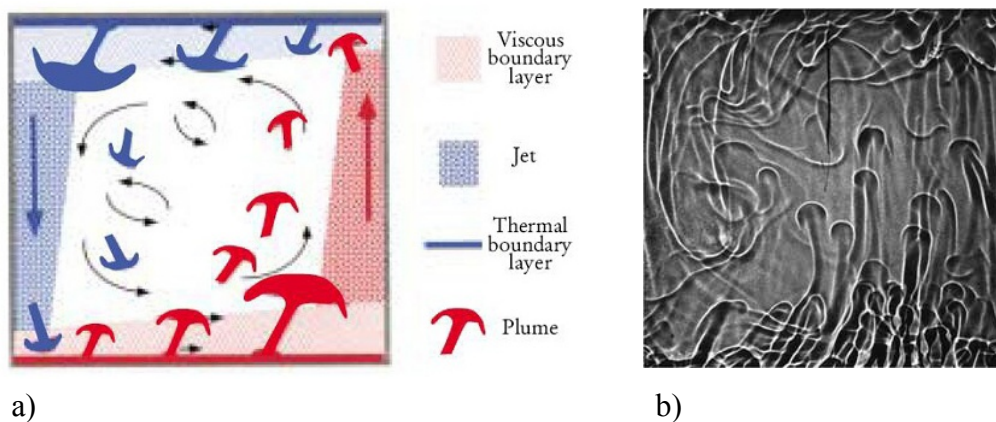a)   b)

Figure 2   Large scale circulation, plumes and jets
a) Schematic representation of large scale circulation, plumes and jets [7]
b) Pattern of the turbulent natural convection of glycerol [7]

Irregular reversals of the wind flow direction have been observed and the reason of such a reversal is not clear. It is supposed that the wind is interactively driven by the rising and falling of large plumes, collection of plumes (Figure 2) or small perturbations that are generated at the bottom and top plates [11]. Lifetimes of bi-directional states of the flow have quantitative statistical analogy with the lifetime of solar flares in the Sun's outer layer [12].

1.3.3 Helium as a working fluid

Cryogenic helium (~ 5 K) is a useful working fluid for experimental studies of natural convection [13]. Helium properties have strong dependences on the pressure and temperature in the vicinity of the He critical point (5.195 K, 227.5 kPa and 69.64 kg/m^3) and cold helium gas has an extremely low viscosity and thermal diffusivity in comparison with other commonly used fluids (air, water, Hg) (Table 1).

Table 1   Fluids properties

Fluid	Temperature	$\alpha/\nu\kappa$
Air	20 °C	0.122
Water	20 °C	14.4
Mercury	20 °C (SVP)	3.43
SF6	50 °C (5 MPa)	$7.5 \cdot 10^5$
Helium (gas)	5.5 K (280 kPa)	$1.41 \cdot 10^8$

This means that Ra number can be varied over a wide range of values and that it is also possible to reach simultaneously very high values of Ra in a relatively small cell filled with cold He gas. Niemela et al. [14] reached Ra of about 10^{17}, which is of the same order of magnitude as for atmospheric turbulence (Table 2). Similar results can be achieved with the heavy gas SF$_6$ but disadvantage of this gas is the necessity of measurement at high pressures (up to 50 MPa at 300 K) for the highest Ra [15].

Table 2 Examples of high Rayleigh number convections

Examples	Ra
Atmosphere	$\approx 10^{17}$
Ocean	$\approx 10^{20}$
Sun	$\approx 10^{21}$

Another important advantage of using He as a working fluid is a very good knowledge of its thermophysical properties [16].

1.3.4 Contradictory experimental results

Evidence of transition towards the Kraichnan regime was claimed by the "Grenoble group" on the basis of experiments with cold He gas. Chavanne et al. [17] observed a power law $Nu \sim Ra^{0.38}$ (Figure 3) and a different behaviour of the He temperature fluctuations above $Ra \sim 10^{11}$ in a cell with aspect ratio $\Gamma = 1/2$. This finding was interpreted as the transition to the Kraichnan regime [18], [19]. They also claimed to have observed the Kraichnan regime above $Ra \sim 10^{11}$ in experiments with three different convection cells (with smooth brass bottom plate, smooth and rough cooper plates) [5]. Recently Grenoble group [20], [21] repeated measurements with the cell

used in previous experiments [19], but with improved thermometry. They confirmed results on *Nu(Ra)* obtained by Chavanne et al. [19] with transition to a new regime at $Ra \sim 10^{11} - 10^{12}$. Gauthier et al. [21] published confirmation of qualitative change in statistics of temperature fluctuations at high *Ra* which was obtained with temperature sensors by one order of magnitude smaller than in [19].

Figure 3   Dependence of the Nusselt number Nu on Rayleigh number Ra and schematic representation of the convection cell [17]

On the other hand, the Oregon group (Niemela et al.) [14] published results for the same aspect ratio $\Gamma = 1/2$, but for a convection cell 5 times higher (Figure 4).
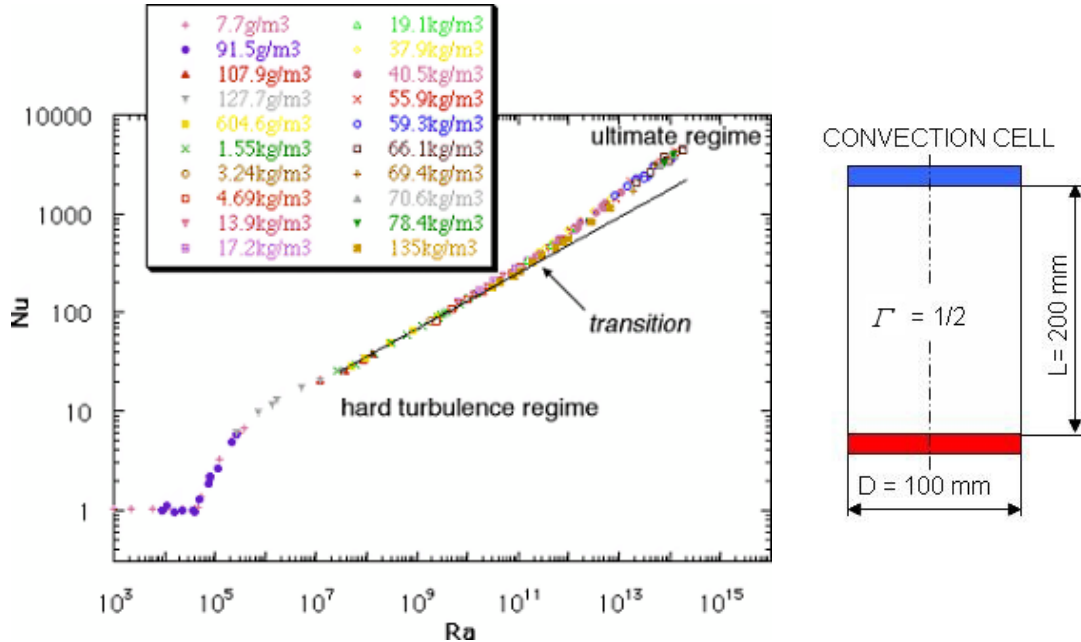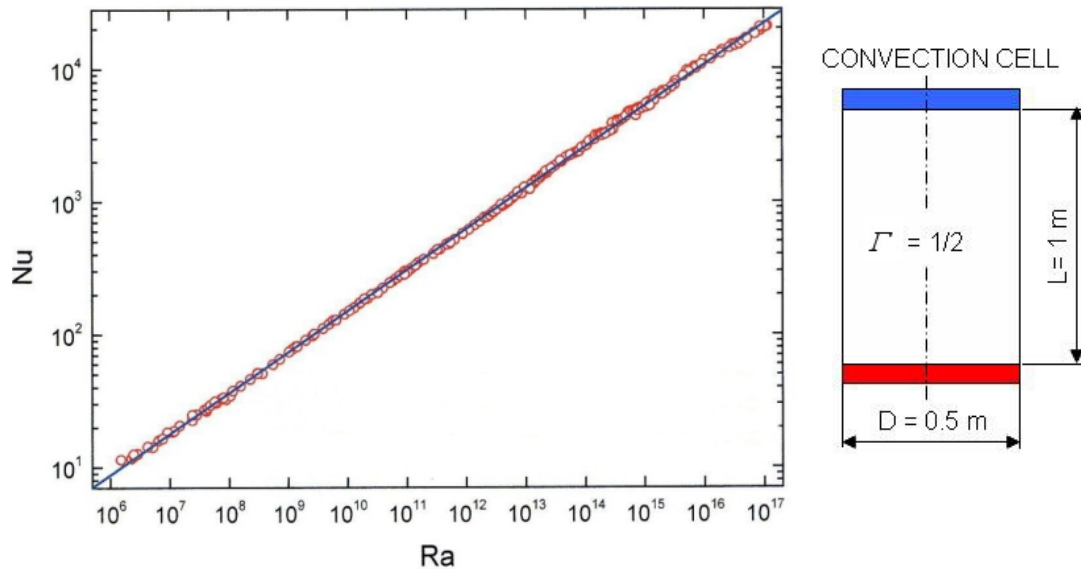

Figure 4   Dependence of the Nusselt number Nu on Rayleigh number Ra and schematic representation of the convection cell [14]

They obtained the dependence $Nu \sim Ra^{0.309}$ in the Ra number range from 10^6 to 10^{17} without any evidence of transition to a different power law. Niemela and Sreenivasan [10], [22] performed additional experiments to check the dependence $Nu(Ra)$ with the aspect ratios $\Gamma = 1$ and 4. Also from those measurements, they obtained a power exponent close to 1/3. In all experiments they measured temperature fluctuations at several positions inside the cell. They observed change in the statistics of temperature fluctuations above $Ra \sim 10^{10}$ [10], [8].

Concurrently with experiments, numerical simulations are being developed. This helps substantially to interpret experiments, and vice versa. Only experiments can confirm the numerical and theoretical models being developed [4], [6], [9], [23], [24].

1.3.5 Parasitic heat fluxes

Experimental data are influenced by the construction details of the cell, such as sidewall conduction, heat conductivity and capacity of the plates, surface roughness of the plates, etc. [25], [26], [27], [12]. Measured data have to be analyzed very carefully.

With increasing precision in the determination of Nusselt number Nu the spurious effects previously neglected have to be taken into account. It has been shown by a numerical model of Ahlers [25] that the conduction of the cell sidewalls may significantly contribute to heat transfer, increase the measured Nu value and thus influence the power law $Nu(Ra)$. Roche et al. [27] derived a simple analytical formula for the sidewall correction as a function of a so called wall number W. This is the ratio of the sidewall conductivity and conductivity of the static gas column in the cell, i.e.

$$W = \frac{2 \cdot t \cdot \lambda_w}{R \cdot \lambda},$$ (8)

where t is the thickness of the sidewall and λ_w its heat conductivity, R and λ are the cell radius and He heat conductivity, respectively. This model is equivalent to the broadening of the effective area of a copper plate by parasitic heating of the fluid from sidewall.

The corrected Nusselt number Nu they derived as

$$Nu_c = Nu_m \cdot \left(1 - A \cdot \sqrt{2} \sqrt{\frac{W}{\Gamma \cdot Nu_m}}\right),$$ (9)

where Nu_m is the measured Nusselt number and the constant A is of order unity.

The previous formula was tested by using the results obtained from three different cells with aspect ratio 1/2: a large thick-wall cell with $W = 3$, a large thin-wall cell with $W = 0.6$ and a small cell, $W = 3$. After the correction, the data obtained from those cells collapsed within 15% error interval into one dependence $Nu(Ra)$ while the uncorrected data differed up to 40%.

A more recent analysis of sidewall effects by Niemela and Sreenivasan [10], based on a numerical model of the relevant fluid-structure and on experimental data, concluded that the corrections can not be precise and that the correction shifts the Nu range downwards by a few percent (this was done for their experiment). This shift diminishes at high Ra and thus the exponent in the power law $Nu(Ra)$ is slightly increased after the correction. Contrary to Roche et al. [27], Niemela and Sreenivasan surmise in their note in [10] that the correction does not depend on the thickness of the wall but on the ratio of the conductivities of the wall material and the gas.

1.3.6 Effect of plates on convection

Constant temperatures at the lower and upper He boundaries of the cell could be ideally maintained by top and bottom plates with infinite heat conductivity and capacity. The influence of the real properties of the plates was analyzed in [26]. On the basis of semi-quantitative considerations, the authors formulated a criterion for possible restriction of plates on convective flow. They solved the Fourier equation for the temperature distribution in the volume of plates. A uniform constant heat flux is generated by a heater at one boundary. At the boundary which is in contact with fluid, a flux simulating the effect of the plumes is imposed. This is simulated by the means of a function that is periodic in time and in coordinates on the plate surface. The amplitude of this function was postulated to be of the order of magnitude of the total heat flux transferred by convection. The space period was approximated by the cell dimension and the time period by the time constant of the heat diffusion through the viscose boundary layer. The solution for the temperature on the plate surface was then found. According to the described analysis, the heat conductivity rather than the capacity of the plates is crucial in experiments with He. The higher is the heat conductivity of the plate the less should be the plate effect on the convection.

The criterion is based on the idea that the temperature fluctuations at the plate surface could restrict the convection when they exceed the fluctuations characteristic for the fluid in the cell volume. For experiments with He they formulated such a restriction criterion as

$$Cr = \frac{\pi^2}{\Gamma} \cdot \frac{a}{L} \cdot \frac{\lambda_p}{\lambda} \cdot \frac{1}{Re \cdot Pr} < 1 \, , \tag{10}$$

where a is the thickness of the plate, λ_p the heat conductivity of the plate, Re the Reynolds number. For high values of Pr they used the approximation $Re \cdot Pr \approx 0.206 \cdot Ra^{0.49} \cdot Pr^{0.3}$.

They applied the criterion Cr in its dependence on Ra numbers for a comparison between published experimental data.

The plates effect was discussed on the basis of numerical model in [4]. The authors compare a scaling law $Nu(Ra)$ simulated numerically for convection ($\Gamma = 1/2$) with experimental data of various laboratories obtained with water and cold He in a cell with copper plates. First, numerical results were obtained for constant temperature at top and bottom boundary in the range of Ra numbers from 10^6 to 10^{14} by Amati et al. [9]. New results for constant heat flux imposed at the bottom boundary in the range of Ra from 10^6 to 10^{11} are presented in [4]. The letter results are very close to the experimental data while the data for constant temperature at the bottom boundary deviate from the measured $Nu(Ra)$ above a Ra of about 10^9. Although those simulations do not describe real plates they indicate a possible effect even of high conductivity copper plates on observed convection at high Ra numbers.

2 Objectives and methods

2.1 Objectives

The aim of the research project is to design, realize and test a helium cryostat with a cylindrical convection cell for investigation of the turbulent natural convection at high Rayleigh numbers ($10^6 < Ra < 10^{15}$). Cryogenic ^{4}He will be used as a working fluid. The work includes cryogenic tests and the preparation of the apparatus for the measurement of the functional dependence of the Nusselt number Nu on the Rayleigh number Ra.

As discussed above, various experiments with cryogenic ^{4}He gas gave controversial results. The cryostat is then to be designed for experiments which should resolve the question about the transition to an ultimate Kraichnan regime within a range of available Ra (sec. 1.2.2).

To achieve this goal the convection cell is to be designed with great emphasis on the minimum influence of the cell structure and materials on the studied convection within the considered wide range of Ra and Nu numbers.

2.2 Methods

It is planned to employ know-how, equipment and technologies of the Institute of Scientific Instruments AS CR, v.v.i. (ISI):

1. The concept of the cryostat NMR III [28] developed at ISI is to be utilized. A newly designed experimental cell is to be implemented in the cryostat.

2. Special technologies of joining and welding (electron beam welding, vacuum brazing and microplasma welding) are at our disposal at ISI to design and manufacture the apparatus.

3. For the cryogenic tests, parts of an old experimental cryostat can be modified and reused.

4. Liquid helium (LHe) supply (recirculated in a recovery system) will be employed as the source of He.

5. For the experiment preparation (operating parameters of the working fluid, He consumption, duration of measurements, etc.) the NIST He database [16] will be used.

3 Analysis of the convection experiment

3.1 Cryostat conception

The cryostat design is based on a low loss cryostats NMR III [28] for a NMR magnet developed and manufactured at ISI. In the centre of the cryostat (Figure 5), the experimental convection cell is placed instead of the superconducting magnet. The cell dimensions and some of the details of its design are derived from the NMR III cryostat dimensions.
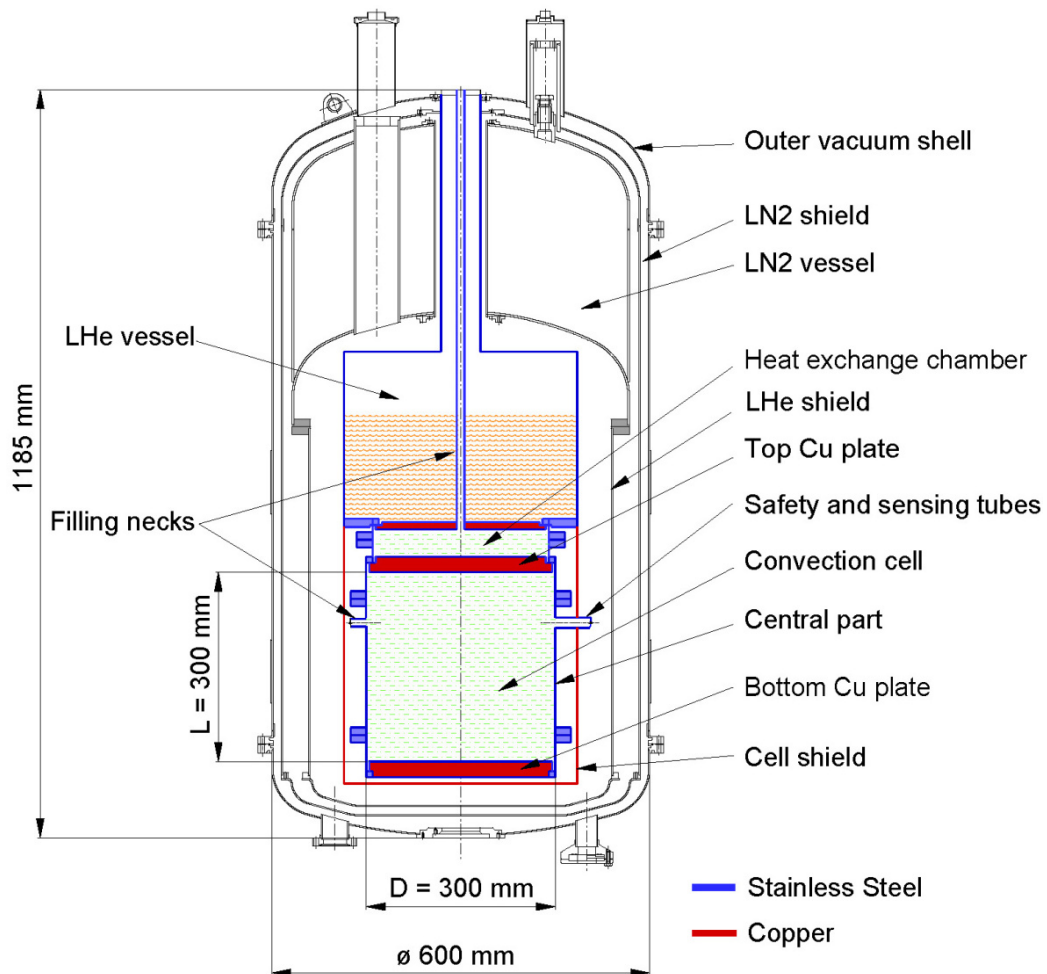
Figure 5   Schematic representation of the cryostat

The convection cell is thermally connected with a liquid helium vessel (LHe vessel) by a heat exchange chamber filled with gaseous He (GHe). The main function of the LHe vessel at 4.2 K in the cryostat is to remove the convection heat flux from the cell.

During all regimes of the experiment, total parasitic heat flux to the convection cell must be negligible in comparison with the measured convection heat flux. The contribution of thermal radiation to this parasitic heat is reduced by a cell radiation shield which is thermally anchored to the liquid He vessel.

In convection experiments the main heat load of the LHe vessel comes from the convection cell and this will be at least one order of magnitude higher than the LHe heat load typical for a NMR cryostat. Thus the LHe vessel and convection cell are shielded

directly by the liquid nitrogen vessel (LN2 vessel) and LHe shield (~ 77 K), contrary to the low loss NMR cryostat, where another shield is inserted between the LHe and LN2 vessels. The radiation heat flux from the outer vacuum shell (300 K) to the LN2 vessel is reduced by a LN2 radiation shield (~ 220 K) that is cooled by cold gaseous nitrogen evaporated from the LN2 vessel.

The cell, heat exchange chamber and LHe vessel are suspended on a central neck inside the outer vacuum shell. High vacuum in the inner space of the cryostat reduces heat fluxes by residual gas. The vacuum is maintained by cryopumping to a pressure lower than 10^{-6} Pa.

3.2 Convection cell conception

The conception of the cylindrical convection cell is schematically shown in Figure 6. The convection cell is divided into three parts. The top and bottom parts are composed of thin stainless steel sidewalls of low heat conductivity and copper plates of high heat conductivity. The middle part is exchangeable.
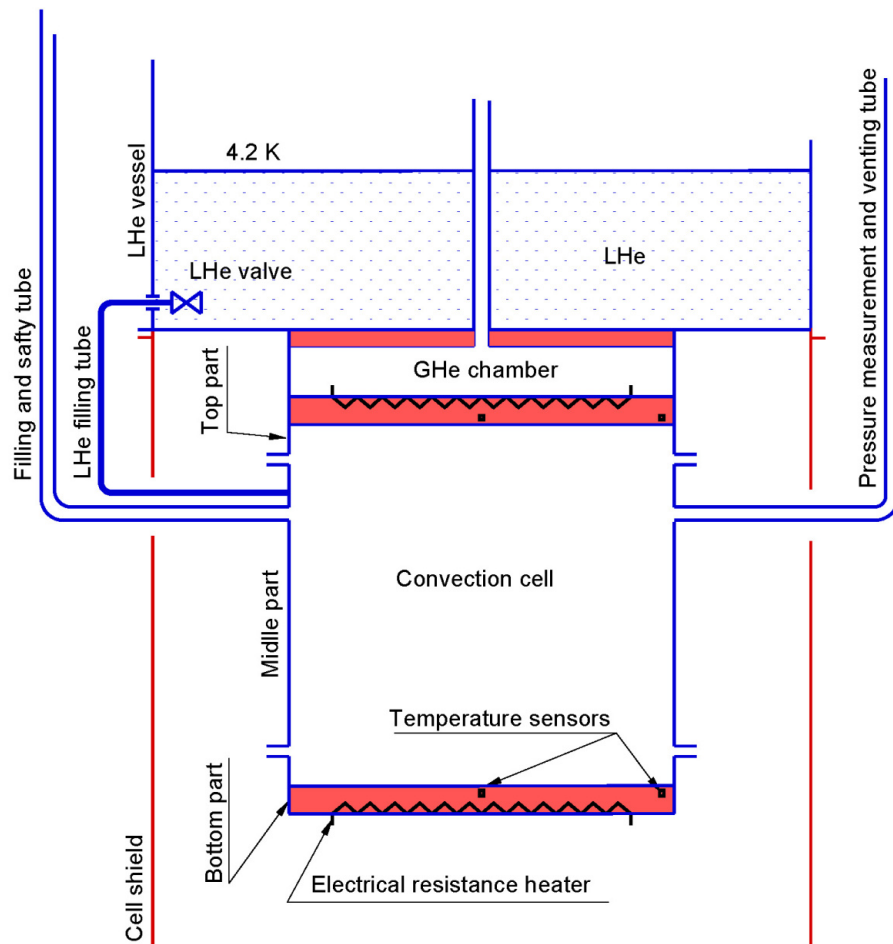

Figure 6   Conception of the convection cell

A stainless steel tube is used for initial cooling procedure of the cell and for venting in the case of accidental overpressure. The second identical tube serves for pressure measurement and for venting of the cell.

The cell is filled by a LHe filling tube during experiments. This tube connects the cell with a LHe valve placed on the bottom of the LHe vessel.

The top and bottom plates are equipped with electrical resistance heaters. The bottom plate heater provides the cell with the convection heat flux. This flux is removed from the top plate of the cell via the heat exchange chamber. The top plate temperature is roughly set by gaseous He pressure in the chamber and the heater of the top plate serves for precise adjustment of this temperature.

The plates temperatures are measured by two sensors embedded near the inner surface of the plates.

3.3   Measurement of $Nu(Ra)$ dependence

Adjustment of the Rayleigh number Ra can be achieved by varying the He fluid density, heat power Q_b (applied to the bottom plate) and temperature T_t of the top plate. The He state is evaluated from the measured temperatures of the plates (i.e. from their mean temperature T) and from the measured pressure in the cell. For the known state of He, the properties α, ν and κ are obtained from the NIST database [16], which is widely used as standard. The Rayleigh number Ra is then evaluated from Eq. (2).

The Nusselt number Nu is calculated from the measured temperature difference ΔT between the plates and heat power Q_b applied to the bottom plate, that is, from Eq. (1).

3.3.1   Measured quantities

Pressure measurement

The pressure p of the gas within the cell is measured by using a Baratron 690A 53T RB transducer with an absolute accuracy of about 0.08 %.

Heat power

The heat input to the bottom plate Q_b is measured by a four-wire technique with accuracy better than 0.5 %.

Temperature measurement

Temperatures of top and bottom copper plates, T_t and T_b, will be measured by calibrated germanium temperature sensors Lake Shore GR-200A-1500-1.4B with an absolute accuracy of 4 mK (uncertainty determined for 95 % coverage probability, i.e. coverage factor k = 2). Thus the uncertainty of the mean temperature $T = (T_t + T_b)/2$ of the He fluids is about 3 mK.

It is planned to stabilise the temperature T_t of the top plate by using the temperature controller Lake Shore 340.

The accuracy of measurement of temperature difference ΔT in the cell was increased by additional comparative calibration of germanium temperature sensors of the top and bottom plates. The uncertainty 2 mK (k = 2) of small values of ΔT was achieved.

3.3.2   Total accuracy assessment

In accordance to the theory outlined in (sec. 1.2.1), a scaling law $Nu \sim Ra^{1/3}$ is expected. This is equivalent to a constant value of the $Nu/Ra^{1/3}$ ratio.

For simplicity the Nu^3/Ra ratio is used for uncertainty analysis in this section, i.e.

$$\frac{Nu^3}{Ra} = \frac{Q_b^3}{\dfrac{\left(\lambda \cdot \dfrac{\Delta T}{L} \cdot S\right)^3}{g \cdot \dfrac{\alpha \cdot \Delta T}{v \cdot \kappa} \cdot L^3}} = \frac{1}{g \cdot S} \cdot \frac{Q_b^3 \cdot \sigma}{\Delta T^4}, \tag{11}$$

where

$$\sigma \equiv \frac{v \cdot \kappa}{\lambda^3 \cdot \alpha} \tag{12}$$

depends on the state of He fluid.

To test the validity of this law we need to know the accuracy of the Nu^3/Ra measurement. The relative uncertainty in this ratio caused by the uncertainties in the determination of individual quantities can be derived as

$$\rho\left(\frac{Nu^3}{Ra}\right) = \sqrt{[3 \cdot \rho(Q_b)]^2 + [4 \cdot \rho(\Delta T)]^2 + [\rho(\sigma)]^2}, \tag{13}$$

where

$$\rho(\sigma) = \sqrt{\left(\frac{\partial \sigma}{\partial T} \cdot \frac{\delta T}{\sigma}\right)^2 + \left(\frac{\partial \sigma}{\partial p} \cdot \frac{\delta p}{\sigma}\right)^2}. \tag{14}$$

The symbols ρ and δ stand for relative and absolute uncertainties, T is the mean temperature of the He fluid and p the pressure inside the cell.

A nearly constant $Nu/Ra^{1/3}$ ratio was observed by the Oregon group over a range of Ra values from 10^6 to 10^{15}. On the other hand, the Grenoble group published $Nu/Ra^{1/3}$ ratio which deviates up to about 40 % from the constant value within the range of Ra values from 10^8 to 10^{12} (Figure 7).
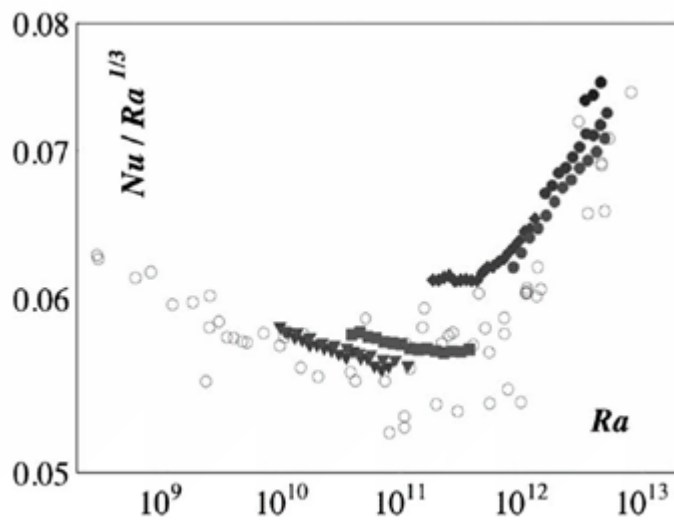

Figure 7   Experimental Ra dependence of Nu/Ra$^{1/3}$ measured by the Grenoble group [5]

This results in more than 100 % deviation in Nu^3/Ra ratio. Measurement accuracy of 20 % in Nu^3/Ra ratio (i.e. 7 % in $Nu/Ra^{1/3}$) was chosen as sufficient for distinguishing such a deviation from constant. Thus in the following text when we speak about "ratio Nu^3/Ra measured with sufficient accuracy" we mean that Nu^3/Ra ratio is characterised by uncertainty less than 20 %.

3.4   Model of the experiment

For the analysis of the convection experiment the SimRBC program was written by using Microsoft Office Excel [37]. Operation parameters for the convection cell, heat exchange chamber and LHe vessel and errors of the measured quantities are approximately predicted by the SimRBC program. The prediction was performed for scaling law with exponent $\gamma \sim 1/3$ published by Niemela et all [14]. This law was used for an estimate of the heat transferred both in the cell and heat exchange chamber. HePak add-in computer program for Excel [39], was used for the calculation of the thermophysical properties of He according to the NIST database [16].

SimRBC Input data:

- Convection cell and heat exchange chamber heights
- Volume of LHe in the LHe vessel
- Density of GHe in the heat exchange chamber
- Uncertainties of quantities measured by sensors
- State of He in the convection cell (mean density and mean temperature)
- Bousinesq condition $\alpha \cdot \Delta T$

Main output data:

- He properties in the convection cell and heat exchange chamber calculated from the database HePak (thermal expansivity, thermal diffusivity, thermal conductivity and kinematic viscosity)
- Pressure in the convection cell and heat exchange chamber
- Heat powers in the heaters at the top and bottom plates
- Time constant τ for the stabilization of the convection
- LHe consumption in the LHe vessel
- Temperatures of the top and bottom plates ($T_t = T - \Delta T/2$, $T_b = T + \Delta T/2$)
- Uncertainty of the Nu^3/Ra ratio produced by the uncertainties of individual quantities
- Ra, Nu and Pr numbers

An example of the results calculated by SimRBC for an experiment with one value of He density (30 kg/m^3) in the convection cell is presented in Appendix 1.

3.5   Experiment analysis in SimRBC

An analysis of the convection experiment to study the $Nu(Ra)$ dependence was performed for the convection cell, heat exchange chamber and LHe vessel (for dimensions see Table 3).

21

Table 3 Dimensions of the convection cell, heat exchange chamber and LHe vessel

	Diameter	Height	Volume
	mm	mm	Litre
Convection cell	300	300	21
Heat exchange chamber	274	50	3
LHe vessel	420	222	30

Aims of the analysis:

- To specify the ranges of the measured quantities (mean temperature and pressure, heat power to the bottom plate)
- To specify the range of the *Ra* and *Pr* numbers
- To specify the influence of measurement uncertainties on Nu^3/Ra

Limitations of the experiment:

- The Boussinesq condition (4) limits the highest values of *ΔT* (and thus the highest *Ra* value). In this analysis the condition $\alpha \cdot \Delta T \leq 0.2$ was applied.

- For high He densities, the lowest value of the mean temperature in the cell is limited by the He condensation temperature in the convection cell on the top plate.

- For low densities, the lowest value of the mean temperature in the cell is limited by the conductivity of the heat exchange chamber. The temperature difference over the heat exchange chamber $(T_t - 4.2\ \text{K})$ is small and the chamber conductivity is not sufficient to remove the convection heat from the cell.

- Near the He critical point and under Boussinesq condition *ΔT* is small and this results in high uncertainty of Nu^3/Ra at high *Ra* values, see Eq. (13).

3.5.1   Results of the analysis

Results of the simulation for various densities of He in the cell are presented in Figures (8-12) where the condition $\alpha \cdot \Delta T = 0.2$ was applied. Only results with the Nu^3/Ra ratio with sufficient accuracy to distinguish controversial results on scaling law are presented (sec. 3.3.2).

Uncertainties of Nu³/Ra

The total relative uncertainty of the ratio Nu^3/Ra, see Eqs. (13-14), caused by uncertainties in the mean He temperature T (3 mK), pressure p (0.1 %), temperature difference *ΔT* (2 mK) and heat power (0.5 %) is shown in Figure 8(a). Contributions of individual quantities from Eq. (13) are presented in Figure 8(b), (c) and (d). All uncertainties in this section are estimated for 95 % covering probability (covering factor k = 2).

From Figure 8(b-d) it is evident that the inaccuracy in the *ΔT* measurement is responsible for the highest contribution to the Nu^3/Ra uncertainty. Even though, to increase the accuracy of the measured temperature difference *ΔT*, Ge sensors were additionally calibrated one relatively to each other with 2 mK accuracy.
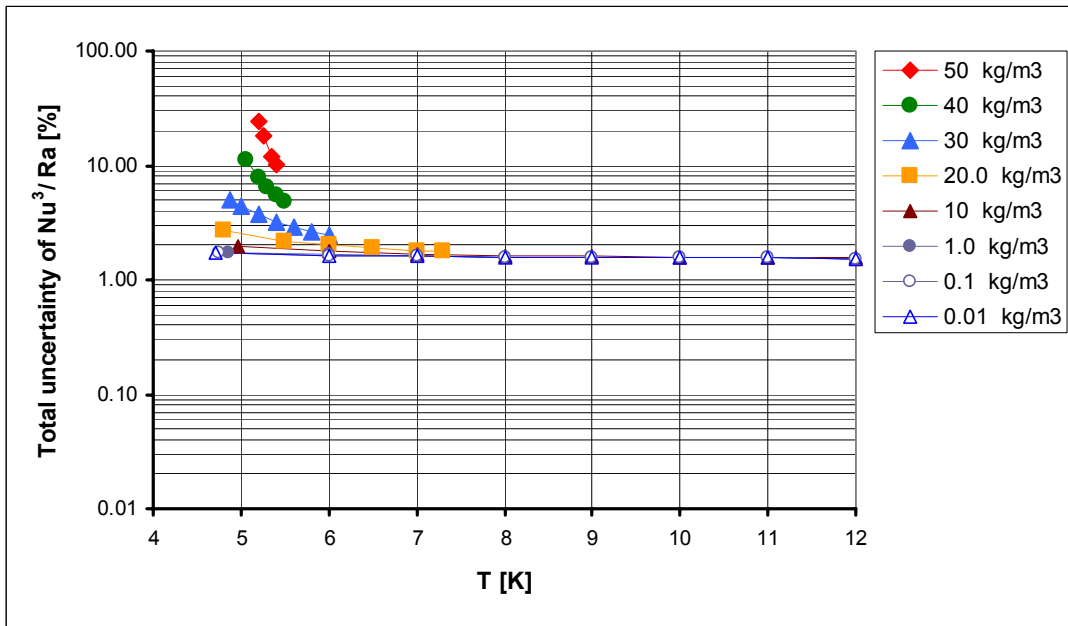
Figure 8   (a): Dependence of the total relative uncertainty in the Nu^3/Ra ratio on the mean temperature T derived from Eq. (13) for various densities and caused by uncertainties in the determination of the mean He temperature T (3 mK), pressure p (0.1 %), temperature difference ΔT (2 mK) and heat power (0.5 %)
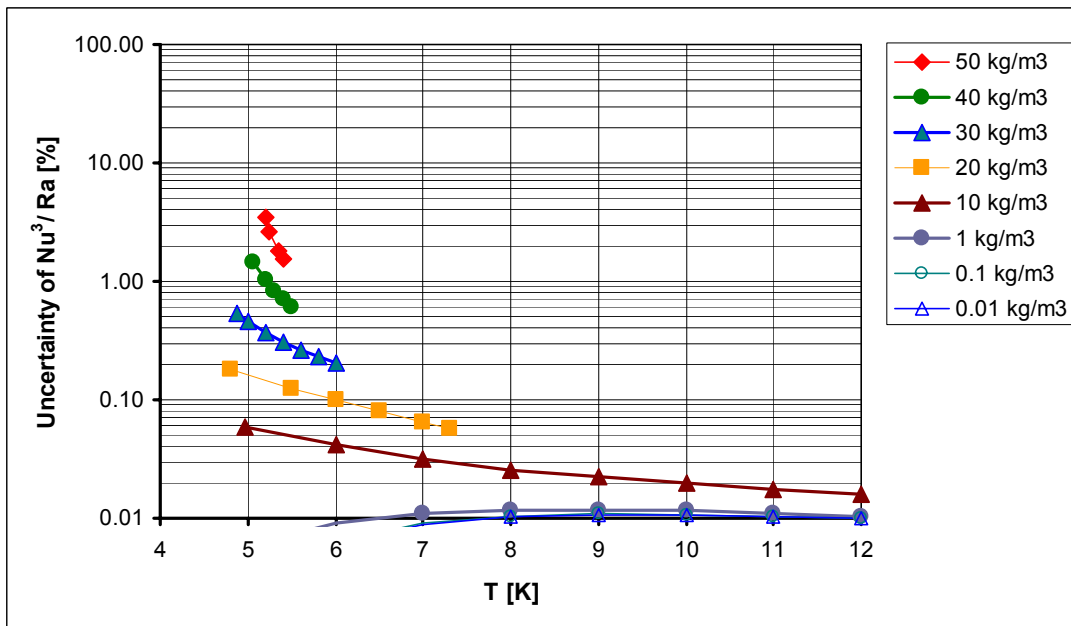
Figure 8   (b): Uncertainty in the Nu^3/Ra ratio corresponding to the mean temperature T uncertainty of 3 mK

23
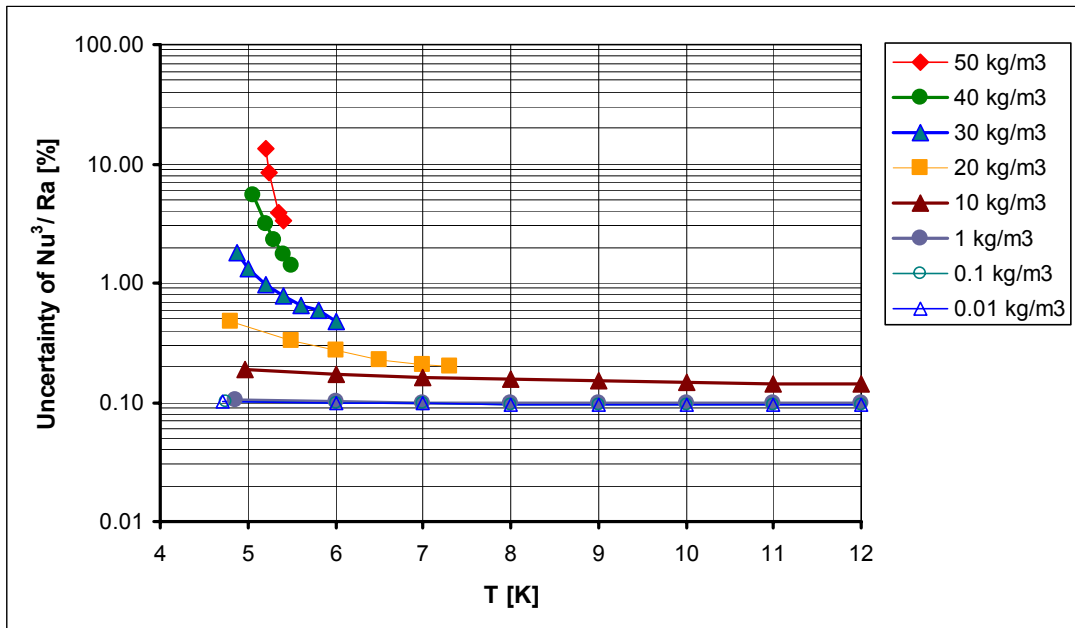
Figure 8   (c): Uncertainty in the Nu³/ Ra uncertainty corresponding to the mean pressure p uncertainty of 0.1 %
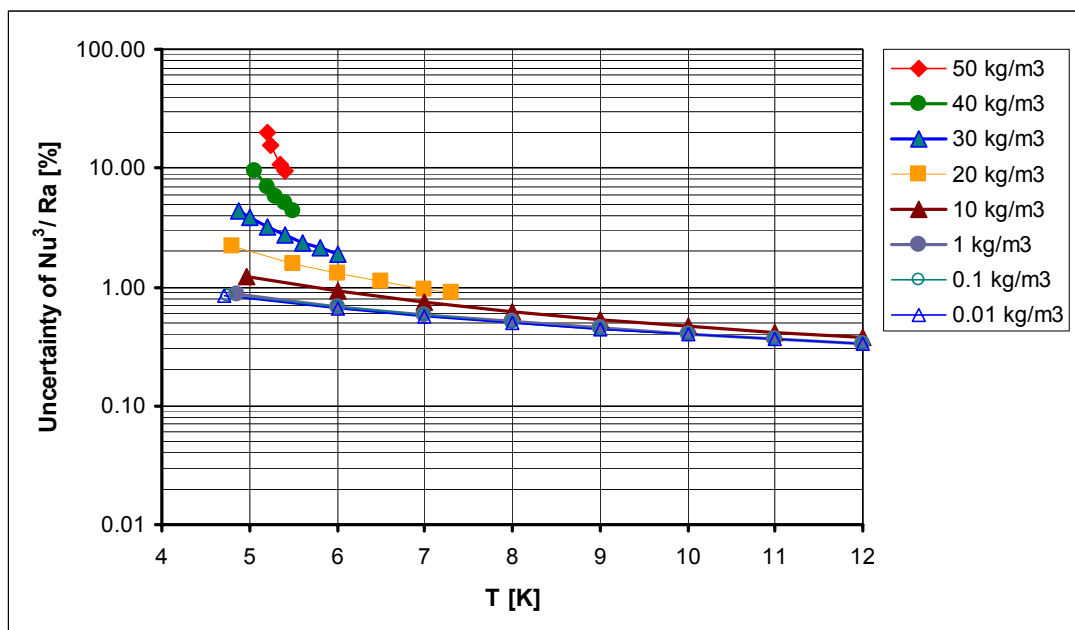
Figure 8   (d): Uncertainty of the Nu3/ Ra ratio corresponding to the uncertainty of temperature difference ΔT of 2 mK

24

Ranges of *Ra* numbers and the measured quantities

The dependence of the *Ra* numbers, calculated from Eq. (2) on the mean temperature *T* and pressure *p* are plotted in Figure 9(a, b).

The highest $Ra = 2.3 \cdot 10^{14}$ in Figure 9(a, b) is predicted to be measured with a total uncertainty of the Nu^3 / Ra ratio lower than 20 % for a 50 kg/m^3 He density, see Figure 8(a). The higher value of $Ra = 10^{15}$ could be achieved with a density of He close to its critical point (~ 70 kg/m^3) but with an uncertainty of 50 %.

Ra numbers decrease with increasing temperature (Figure 9(a)). The maximum temperature at which convection can be studied is limited by the maximum operating pressure.

Ra numbers decrease with increasing pressure *p* for a given He density (Figure 9(b)). For design reasons, a lower pressure in the cell is preferred: the value of the maximum operating pressure of 250 kPa was chosen as sufficient for high *Ra* experiments.
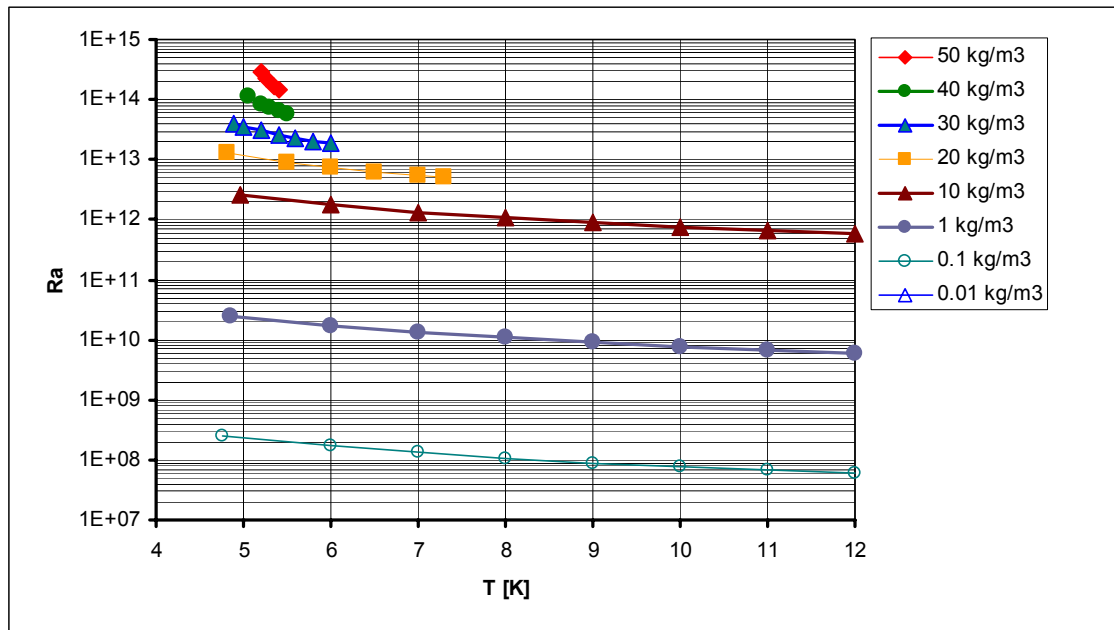
Figure 9   (a): Calculated Rayleigh number Ra dependence on the mean density and temperature T of He in the experimental cell (L = 300 mm). For the prediction of Ra number values the Boussinesq condition α·ΔT = 0.2 and the scaling law with exponent γ ~ 1/3 were used

Generally, the *Nu* number depends both on the *Ra* and *Pr* numbers. A domain in Pr-Ra plane was estimated, in which Nu^3/Ra is measured with sufficient accuracy and simultaneously the Boussinesq condition $\alpha \cdot \Delta T < 0.2$ is valid. This domain is approximately demarcated by the upper and lower curves in Figure 10.

The curves define the region in which the influence of the Prandtl number on the observed convection can be tested.
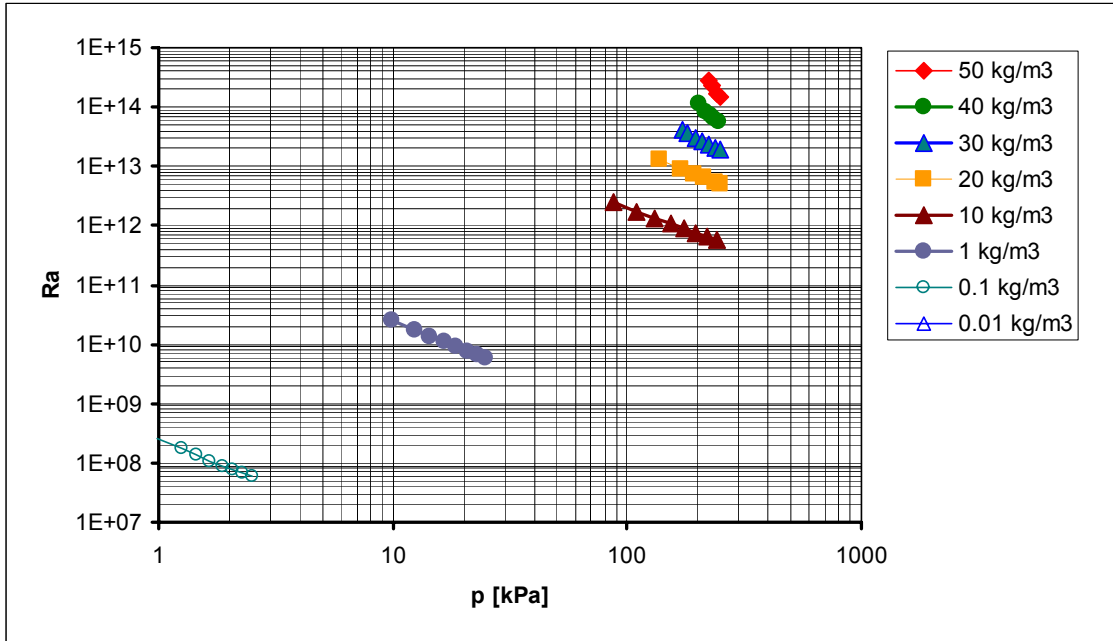
Figure 9   (b): Rayleigh numbers from Figure 9 (a) presented in dependence on He pressure p and mean density
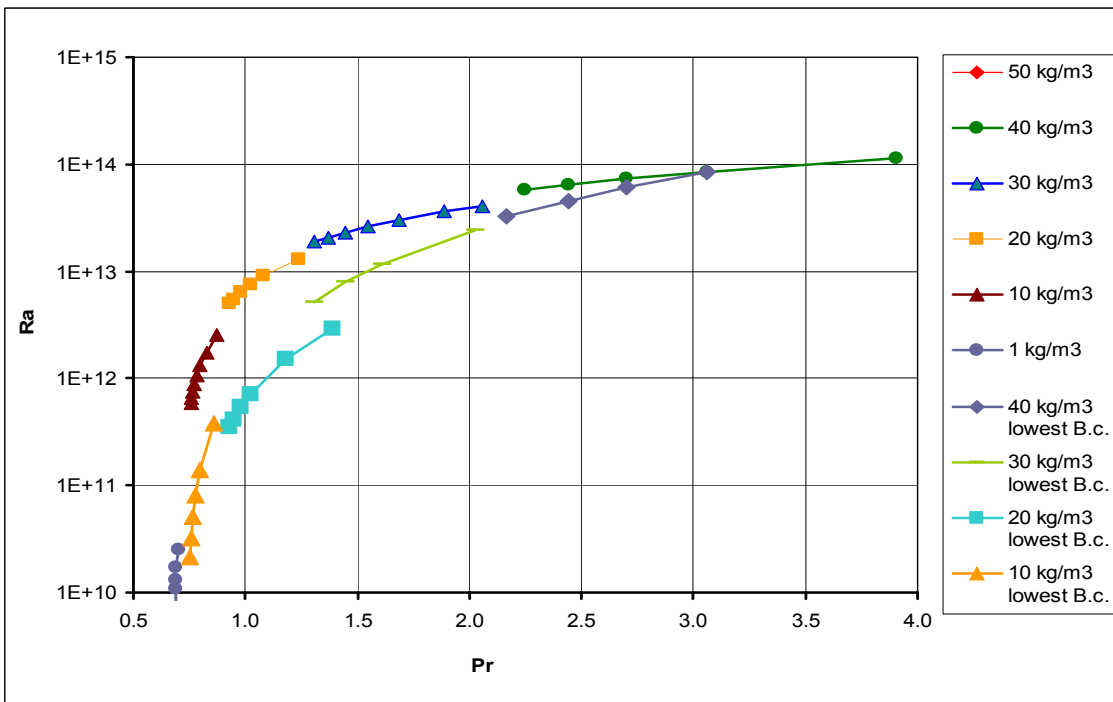
Figure 10   Ra and corresponding Pr numbers are plotted for a model experiment for scaling law with exponent γ ~ 1/3. The upper (Boussinesq condition α·ΔT = 0.2) and lower (lowest B.c.) curves define the region of points where the Nu^3/Ra dependence can be measured with sufficient accuracy.

For the highest densities (10 kg/m^3 – 50 kg/m^3), that is for highest values of *Ra*, the highest heat power to the bottom plate Q_b in the range from 1 W to 5 W is necessary when approaching a pressure of 250 kPa (Figure 11).
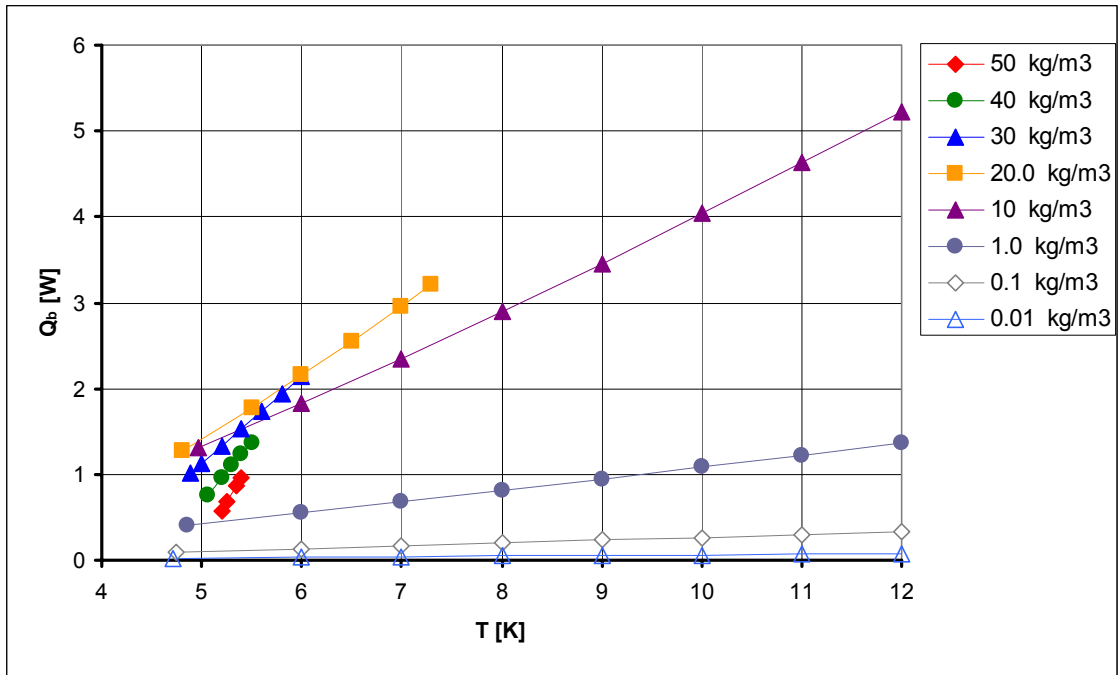
Figure 11   Dependence of the heat power Q_b to the bottom plate on the mean temperature T

Values of He state quantities in the experiment

The ranges of He state quantities (mean density, pressure and mean temperature) in the convection cell and heat exchange chamber obtained by the analysis are summarised in Table 4.

Table 4 Values of state quantities of He in the cell and heat exchange chamber

Convection cell

Density	from 0.01 kg/m^3 to 50 kg/m^3
Pressure	from 100 Pa to 250 kPa
Temperature	from 4.2 K to 12 K

Heat exchange chamber

Density	from 0.1 kg/m^3 to 15 kg/m^3
Pressure	from 1 kPa to 90 kPa
Temperature	from 4.2 K to 9 K

Time of convection stabilization

Let us assume that the convective heat transfer in the cell is limited only by the boundary layers at plates, as described in section 1.2.1. Than the fluid can be modelled as a thermal resistor (thin boundary layers) and thermal capacitor (most of the fluid in the cell). In this model the volume of fluid with thermal capacity $\sim\rho\,S\,L\,C_p$ is heated through the thermal resistor $h / (\lambda\,S)$ with heat power Q_b applied to the bottom plate.

The temperature T_t of the top plate is kept constant. Thus the equation for time dependence of value $\Delta T = T_t - T_b$ approaching its steady-state value can be derived as

$$\frac{d\Delta T}{dt} + \frac{\Delta T}{\tau} = \frac{2 \cdot Q_b}{\rho \cdot S \cdot L \cdot C_p} \qquad (15)$$

where the time constant τ is given by the relation

$$\tau = \frac{\rho\, C_p\, L\, h}{\lambda} = \frac{L^2}{2 \cdot \kappa \cdot Nu} \; . \qquad (16)$$

Here h stands for the boundary layer thickness $h = L / (2\, Nu)$, ρ, κ and C_p are the density, thermal diffusivity and specific heat capacity at constant pressure of He, respectively.

Deviation of the value ΔT (and thus deviation of T_b) from the final steady state is then described by the exponential decay

$$\Delta T \cdot e^{-t/\tau} \qquad (17)$$

where t is the time and ΔT is typically less than 1 K. The setting of the steady-state with an accuracy of 0.1 mK requires a time $t \sim 10\tau$.

The time of steady-state setting increases with the He density in the cell and varies from minutes to hours, see Figure 12(a).

Figure 12   (a): Estimated time (10τ) for the setting of the steady-state temperature Tb at the bottom plate with an accuracy of about 0.1 mK

LHe consumption

The convective heat flux is transferred into the LHe vessel and evaporates LHe. The consumption of LHe increases with increasing density and temperature of He in the cell (Figure 12(b)). The LHe consumptions are calculated for the time 10τ which is necessary to stabilize the convection. For $Ra = 1.5 \cdot 10^{14}$ (He density of 50 kg/m^3 at 5.4 K) the LHe consumption is 11.5 litres during the stabilization time of 4.5 h. The proposed LHe vessel volume of 30 litres (Table 3) is therefore sufficient for the convection experiment.

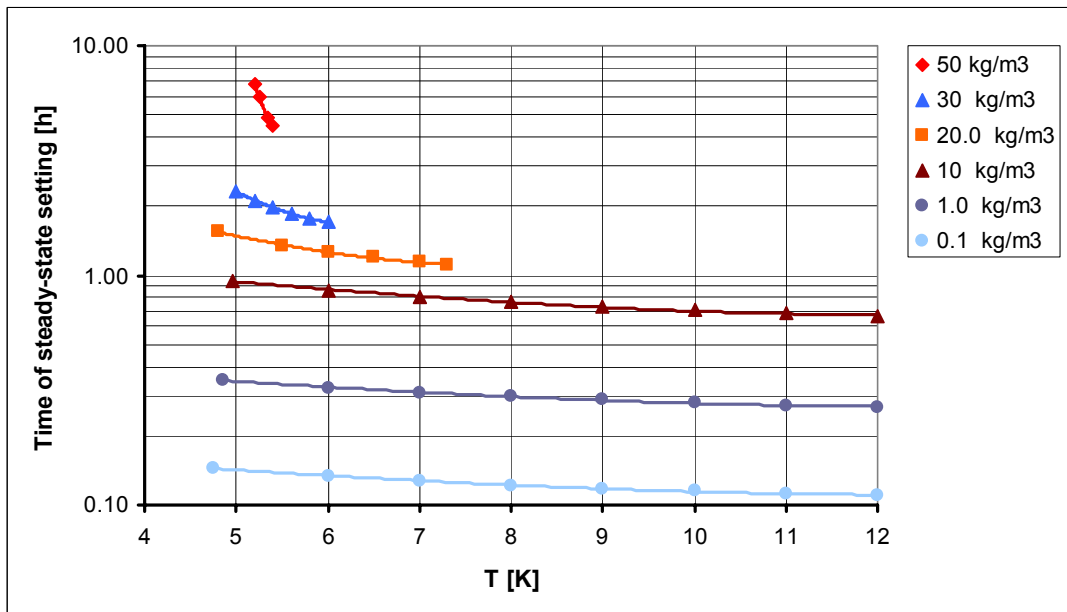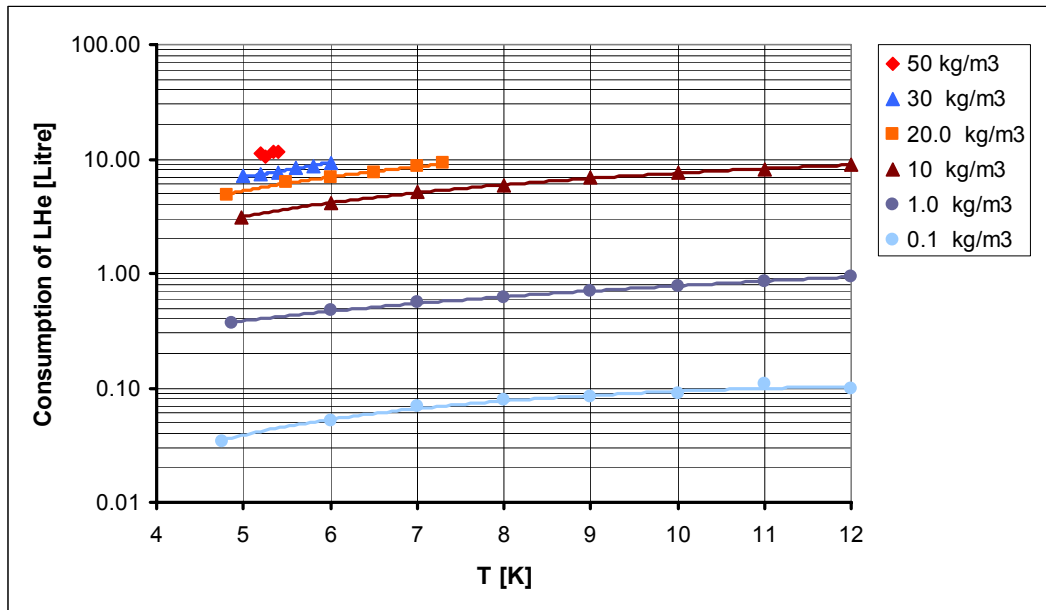*Figure 12   (b): Consumption of LHe during the time t = 10τ for the setting of the steady-state temperature T_b at the bottom plate with an accuracy of about 0.1 mK*

4   Design of the cryostat

The cryostat design is based on the low loss NMR III magnet cryostats as described in section 3.1. In comparison with NMR III cryostats [28], the LHe vessel was completely changed (Figure 5). The outer shell, LN2 shield and LN2 vessel were partly modified without changing their dimensions.

In order to achieve easy assembly of the cell in the cryostat, the outer shell, LN2 shield and LN2 vessel were divided into three parts. The middle part of the outer shell was fitted with flanges and sealed by a rubber o-ring. The middle parts of the LN2 vessel and LN2 shield were bolted together with their respective upper parts to ensure good thermal contact.

The design of the convection cell, heat exchange chamber and LHe vessel partially resulted then from the NMR III cryostat and from the analysis of experiment performed using the SimRBC program described in section 3.5.

4.1   Construction materials of the cryostat components

The materials of all components of the cryostat are chosen with respect to their mechanical and thermal properties. Materials characterized by a f.c.c. crystal lattice, such as copper, aluminium, their alloys and austenitic stainless steel, remain ductile and tough over the entire cryogenic temperature range. Classical iron steels are not suitable for devices used at cryogenic temperatures, because they have a tendency to crack.

Austenitic stainless steel was used for most parts of the outer shell, LHe vessel, heat exchange chamber and convection cell. Good weldability, solderability and mechanical strength were crucial in the choice of the stainless steel material.

The LN2 vessel and LN2 radiation shield are made of aluminium alloy, the cell radiation shield of copper. Aluminium and copper have specific heat capacity of about two orders of magnitude lower than stainless steel and concurrently by two and more orders of magnitude higher heat conductivity. The cooling and temperature stabilization of the parts made of these materials are then more effective. The advantage of aluminium, which was used for the LN2 vessel, is its light weight in comparison with stainless steel and copper (approximately three times lower density).

To decrease parasitic heat fluxes during the experiment it is necessary to minimize the radiative heat exchange between the inner parts of the cryostat. This was achieved by chemical polishing of the aluminium and copper surfaces (LN2 shield and vessel, cell shield).

The thermal emissivity of the outer shell made of stainless steel was decreased by a inner side lining made of a thin aluminium sheet. Stainless steel tubes were wrapped in aluminized Mylar foil. The emissivity values of a stainless steal surface are several times higher than those of an Al alloy surface and about ten times higher than a chemically polished surface made of technically pure copper [29].

4.2   The convection cell and heat exchange chamber

Target convection cell parameters

Ra number up to about 10^{15} under Boussinesq condition $\alpha \cdot \Delta T \leq 0.2$

- cylindrical experimental cell of 300 mm in diameter D and up to 300 mm in height L
- cylindrical cell with the top and bottom plates made of high conductivity copper
- sidewalls with low heat conductivity (to reduce substantially parasitic heat flux)

- the cell design allows to change the aspect ratio $\Gamma = D/L$ from 1 to 2.5 or to implement a middle part with a modified geometry
- operating pressures in the cell from 100 Pa to 250 kPa at temperatures from 4.2 K up to about 12 K
- electrical resistance heaters, placed in grooves on the plates, heat power from 10 mW to 10 W

The cylindrical convection cell consists of three parts, the bottom, middle and top part (Figure 13) [30], [31]. The grey components are made of stainless steel, the coloured pieces of copper. This configuration allows to make exceptionally thin sidewalls of the bottom and top parts and thus to reduce a parasitic heat flux through the walls from the copper plates.

The middle part is exchangeable and allows to vary the cell aspect ratio Γ.
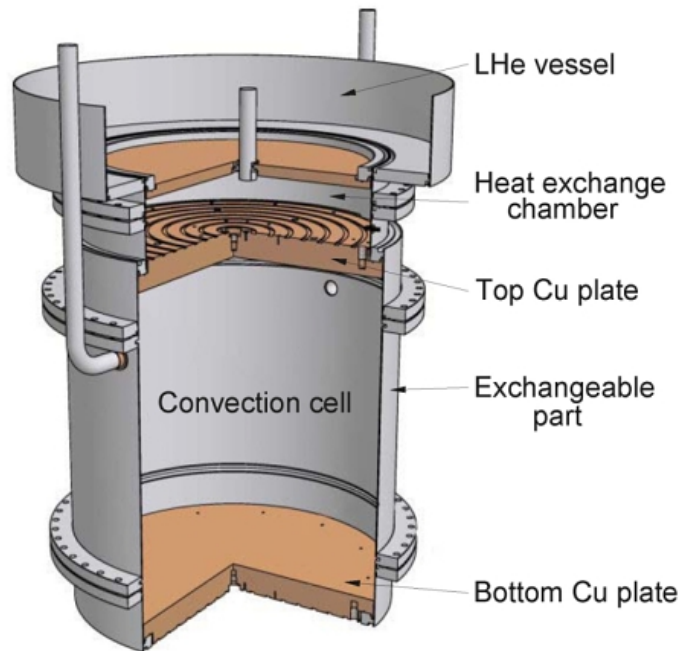
Figure 13   Three-dimensional section of the convection cell with the heat exchange chamber and part of the LHe vessel.

4.2.1   Sidewalls of the cell

The main temperature drop in the cell is in the boundary layers and adjacent sidewalls. The height of the thin cylindrical sidewalls of the bottom and top parts should be higher at least than the supposed thickness of the boundary layer $\delta = L/(2 \cdot Nu)$. Thicknesses of the boundary layers for various Ra and Nu numbers are listed in Table 5. A height of 35 mm of the "thin sidewalls" was then chosen. On the other hand the lower the sidewall, the thinner it can be from a structural point of view.

Table 5 Estimated thickness of the boundary layers

Ra	10^5	10^7	10^9	10^{11}	10^{13}	10^{15}
Nu	4	18	75	311	1290	5351
δ [mm]	34	8	2	0.5	0.12	0.028

4.2.2 Copper plates

The plates of the convection cell are made of oxygen free high conductivity copper (OFHC copper from Outokumpu company). The plates are 300 mm in diameter and are 28 mm thick. The internal surfaces of the plates are machined by soft lathe-turning. The guaranteed roughness of the surfaces is $R_a = 1.6$ μm. This is one order of magnitude lower than the lowest thickness of the boundary layer at $Ra \sim 10^{15}$ (see Table 5). In fact, the roughness could influence the measured $Nu(Ra)$ dependence if it is comparable to the boundary layers thickness.

4.2.3 Heaters of the plates

The plates are heated by heaters made of resistance wires. For these wires suitable grooves are milled on the external sides of the plates. The grooves are designed in spiral shape (Figure 14).

Temperature homogeneity better than 1 mK on the internal surfaces was determined from numerical simulation of the proposed resistance heaters.

The resistance heaters of the copper plates are designed for a 10 W maximal power at 50 V. A constantan wire of 0.14 mm diameter, 32.5 Ω/m specific resistance and 7.5 m length is used for each copper plate. The maximal current of the heaters is 0.2 A.

To ensure good thermal contact the resistance wires are wound up to the grooves and glued by a special cryogenics varnish. The bifilar method of winding is used.
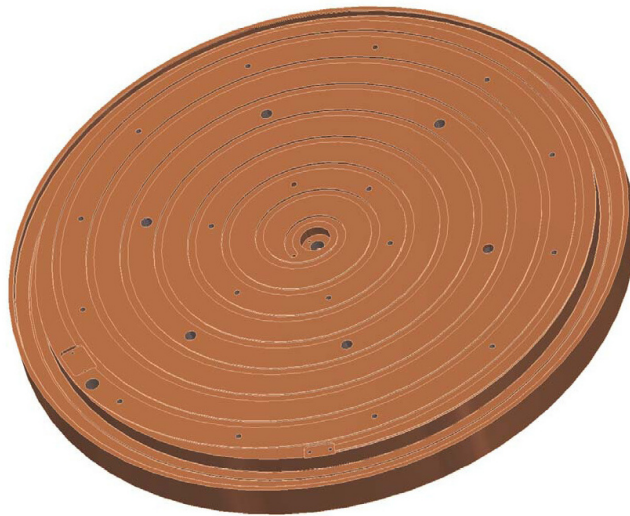
Figure 14   Copper plate

4.2.4 Construction joints and the technology

The thin bottom sidewalls are connected to the copper plates via stainless steel rings (Figure 15). These are brazed to the copper plates on their external sides. Stainless steel sidewalls are microplasma welded to the rings.

The bottom parts are connected to the middle part by demountable flanges. The joints of these flanges are sealed by indium wires.

The convection cell is connected to the LHe vessel via the heat exchange chamber by demountable flanges. The lower part of the heat exchange chamber is a component of the top part of the cell, the upper part is a component of the LHe vessel.
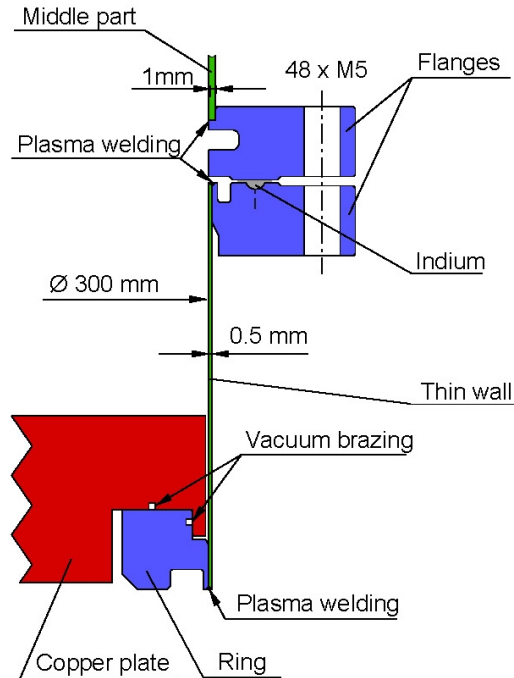
Figure 15   Design and technology of the joints

4.2.5   Strength analysis of the convection cell

The convection cell was designed to be tested at an inner overpressure of 350 kPa which was assessed according to Czech technical standard for high pressure vessels (ČSN 69 0010 standard - Stable pressure vessels) [32]. During the tightness test of the cell (done by using a He leak detector) the cell is to be evacuated and thus exposed to an outer overpressure of 100 kPa.

The copper plates of the top and bottom parts

Material: annealed OFHC copper

Mechanical stress and maximal deflection of the copper plate was calculated for a simply supported circular plate under a uniformly distributed load. Both quantities were evaluated for the inner overpressure of 350 kPa. The plates are of 300 mm in diameter and 28 mm in thickness.

Results:

- Mechanical stress: 16 MPa (yield strength of Cu is about 60 MPa)
- Maximal deflection: 0.07 mm

Cylindrical sidewalls of the bottom parts

Material: austenitic stainless steel

The sidewalls are of 300 mm in inner diameter and 35 mm in height. Due to the design and structural reasons a thickness of 0.5 mm was chosen for sidewalls. The minimal thickness of the sidewalls is limited by the allowable outer overpressure, as the cylinder walls can collapse by effect of elastic instability.

Resulting allowable pressures for the sidewalls are:

- Inner overpressure: 360 kPa
- Outer overpressure: 110 kPa

Middle part of the cell

Material: austenitic stainless steel

The middle part is 300 mm in diameter and 211 mm in height. A thickness of 1 mm for the wall was chosen from structural reasons.

Resulting allowable pressures for the middle part:

- Inner overpressure: 730 kPa
- Outer overpressure: 110 kPa

The main flanges of the cell

The main flanges are sealed by indium wires which requires a permanent preload at all working states. As indium is a minimum elastic material thus the preload has to be provided by the blades of the flanges.

During the experiment the flanges are exposed to forces from pressure varying from 100 Pa to 250 kPa and to the stresses produced by the temperature contractions during the cooling to the LHe temperature (4.2 K). The vacuum tightness of the indium joints has to be assured at the 350 kPa test pressure at LHe temperature.

The calculation of the mechanical stresses and deformations during the cooling would be very complicated, as the temperature time behaviour of the flanges is difficult to define. Therefore, the calculations were performed at room temperatures only.

An initial design for the flanges was proposed (Figure 16) and a preliminary calculation was performed according to the ČSN 69 0010 standard, part 4.18. Since this standard does not prescribe the properties for indium seals, the dimensions of flanges, number and parameters of screws ($36 \times M6$) and tightening torques (4.2 Nm) were those specified for aluminium seals.

The preliminary results were checked by FEM computations performed by the SVS FEM company in Brno. This company is the leading computing and training centre for the ANSYS software (finite element method software for structural analysis) in the Czech Republic.

The FEM computations led to the necessity of increasing the number of screws from 36 to 48 and concurrently to the possibility of decreasing their diameter from 6 mm to 5 mm. The geometry of the flanges should also be slightly altered.

For the new configuration a screws prestress of 2400 N without inner overpressure (at the assembly of flanges) was evaluated. The calculated prestress value guarantees that a permanent deformation of the flanges will not be reached at the test pressure of 350 kPa.
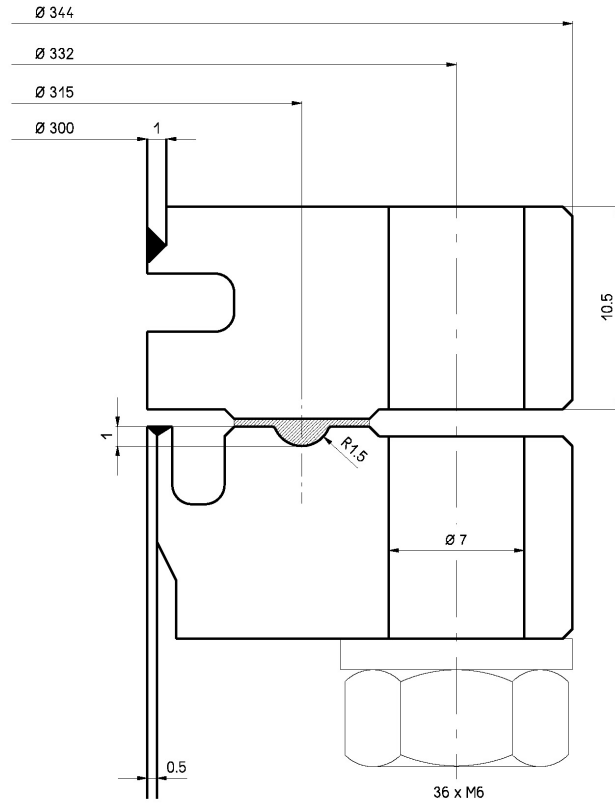
Figure 16   Design of flanges

4.3   LHe vessel

The LHe vessel is designed for an inner overpressure of 110 kPa. During the tightness test of the LHe vessel (done by using a He leak detector) the vessel is evacuated and thus exposed to an outer overpressure of 100 kPa.

The lower bottom part of the LHe vessel is made of two plates (Figure 13). The peripheral plate is made of stainless steel and is plasma welded to the cylindrical wall. The inner plate is made of copper and creates the upper part of the heat exchange chamber. The upper and lower bottoms of the LHe vessel were computed as simply-supported circular plates under a uniformly distributed load. Mechanical stresses and relevant deflections were evaluated for the inner overpressure of 110 kPa.

Upper bottom plate

Material: austenitic stainless steel

The bottom is 420 mm in diameter and 15 mm in thickness.

Results:

- Allowable overpressure: 620 kPa
- Mechanical stress in the material: 40 MPa (the stainless steel yield strength is about 200 MPa)
- Maximal deflection: 0.4 mm

The copper plate of the lower bottom part

Material: copper

The plate is 247 mm in diameter and 10 mm in the thickness.

Results:

- Allowable overpressure: 180 kPa
- Mechanical stress in the material: 21 MPa (the Cu yield strength is about 60 MPa)
- Maximal deflection: 0.16 mm

Cylindrical wall

Material: austenitic stainless steel

The cylindrical wall has a 420 mm inner diameter, 240 mm height and 1 mm thickness.

Resulting allowable pressures:

- Inner overpressure: 520 kPa
- Outer overpressure: 170 kPa

4.4   Heat flux analysis of the cryostat

The heat flux analysis was performed to estimate parasitic heat fluxes to the vessels with cryoliquids (LN2 and LHe vessels) in the pause between experiments, when the plates are not heated. Another aim was to analyse parasitic heat fluxes to the convection cell during experiment (Figure 17, Table 7).

4.4.1   General

The heat transfer in the cryostat consists of radiative heat transfer between the internal surfaces and of conductive heat transfer through the residual gas in the vacuum space, through the necks, supporting solid straps and current leads.

Heat transport in the necks

This heat transport consists of:

- Heat conduction in the neck wall and in the gas inside the neck
- Heat exchange between the gas and the wall
- Radiation heat exchange between the external surface of the neck and the surroundings

As the speeds of the evaporating gas are low, we assume perfect heat exchange between the gas and neck wall (no radial temperature gradient) [33].

Radiative heat transfer

Heat radiation between the surfaces inside the cryostat relates to the thermal radiation properties of the surfaces, emissivity and absorptivity. We suppose isothermal surfaces of the vessels and radiation shields as a result of the high thermal conductivity of Al and Cu shields.

Heat conduction in supporting straps

The cryoliquid vessels and radiation shields are mutually fixed by using straps of low heat conductivity and high mechanical strength. The straps are made of a fibreglass and epoxy resin composite. The heat flux in the straps is significant mainly in the case of the LHe vessel and it should be consequently included.

Heat exchange in residual gas

At low pressures, the thermal conductivity of the residual gas is proportional to the pressure. In the pressure range of about $10^{-4} - 10^{-5}$ Pa the heat exchange is comparable with other sources of heat flux but is negligible at pressures lower then 10^{-6}. The fact that the heat exchange by the gas can be neglected was indirectly verified by the good agreement between the measured parameters of the NMR cryostat manufactured at ISI and those calculated by using the methods described [33]. We can then neglect the heat transport by gas in the cryostat with the convection cell.

4.4.2   Calculations

The heat fluxes inside the cryostat (Figure 17) were calculated by using the KRYOM 3.3 software [38]. The calculation is based on numerical procedures developed for thermal analysis of cryostats [33]. We used the following nomenclature in the heat flux analysis of the cryostat:

QN heat transport in the neck segment, (where QNB and QNE represent the heat fluxes at the upper and lower ends of the neck segment, respectively

QR radiative heat between surfaces

QS heat flux to the thermal anchor (i.e. to the cryogenic liquid used as a heat sink)

QC heat conduction in the supporting straps

QH heat flux through the current leads together with the Joule heat generated by the current

QL total heat input for the LHe and LN2 vessels

TS radiation shield temperature

L length of the neck segment

Numerical symbols represent different cryostat segments.

The cryostat can be divided into two independent subsystems: the LHe subsystem (temperatures between 4.2 K and 77 K) and LN2 subsystem (temperatures between 77 K and 300 K). By knowing the individual heat fluxes the total heat load QL and consumption of cryoliquids can be calculated. The results for the heat flux analysis of both systems are summarized in the Table 7.
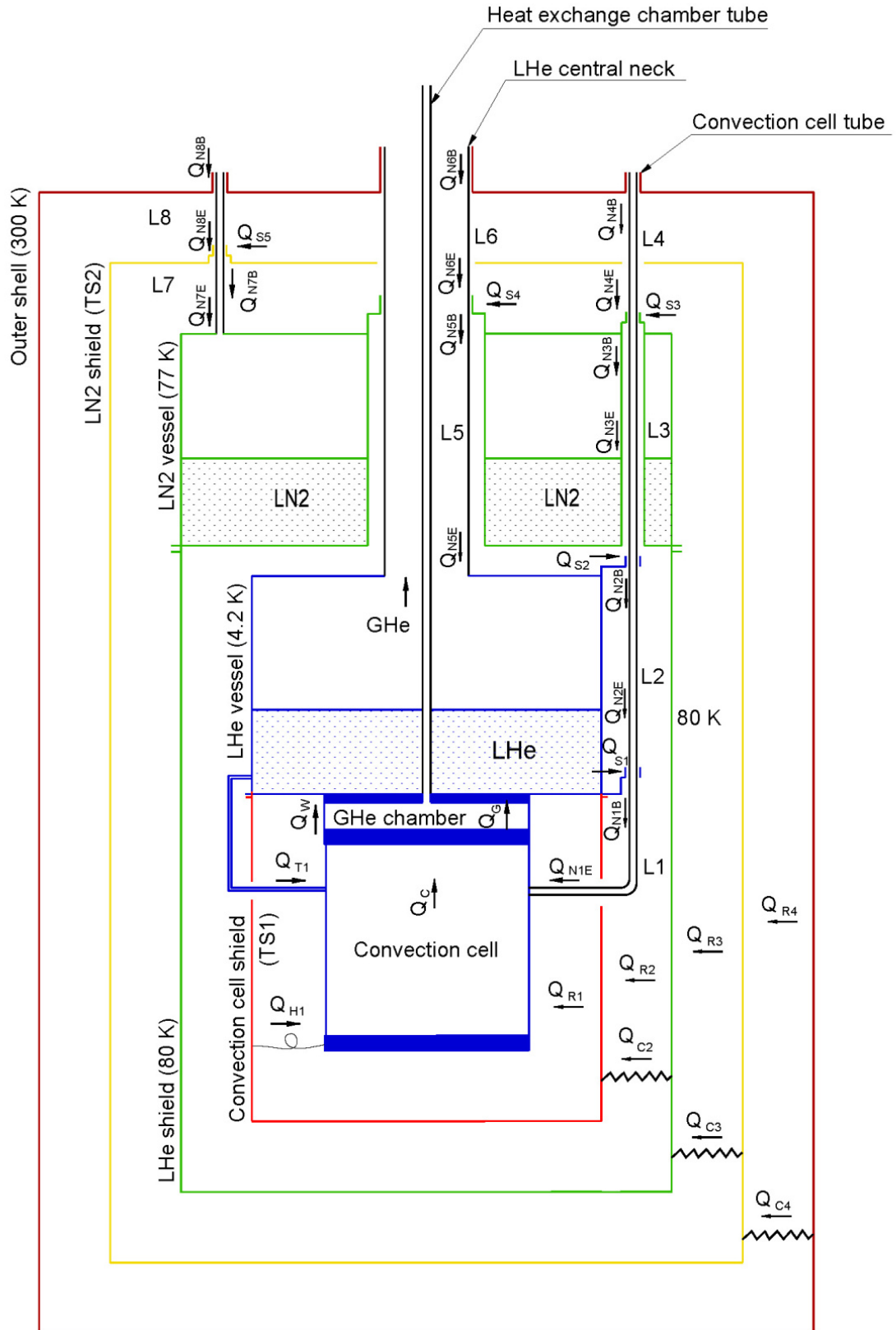
Figure 17   Heat fluxes inside the cryostat

4.4.3 Heat flux analysis of the LHe subsystem

The LHe subsystem consists of the LHe vessel together with the central neck segment *L5*, the convection cell, the convection cell shield and the segments *L1*, *L2* and *L3* of the convection cell tubes. The temperature at the boundary of the LHe subsystem is 77 K. The total heat load *QL* into the LHe vessel is given by the sum of individual heat fluxes, that is, $QL = QN5E + QR2 + QC2 - QS1 - QS2 + QN1E$. The meanings of all terms is evident from the nomenclature described above and in Figure 17.

Convection cell tubes

The convection cell tubes in the LHe system are divided into three segments, *L1*, *L2* and *L3*, by two thermal anchors connected to the LHe vessel at a temperature equal to 4.2 K (Figure 17). As a first step, the heat fluxes *QN* through the neck have to be calculated. The heat fluxes *QS* to the LHe vessel through the thermal anchors can then be evaluated.

For example, the thermal anchor between the *L2* and *L3* segments creates a thermal node in which the heat flux balance is $QN3E - QN2B + QS2 = 0$. The heat flux $QS2 = QN1B - QN2E$ to the thermal contacts can then be calculated. It is possible to calculate the heat flux *QS1* in the same way.

Example of segment L3 analysis in KRYOM

The convection cell tubes are made of stainless steel. Their inner diameter is 14.4 mm and the tubes wall thickness is of 0.15 mm. Static He gas is inside the tubes. The upper end of the *L3* segment of 365 mm length is connected to the LN2 vessel with a temperature equal to 77 K (*TBeg*). The lower end is connected to the LHe vessel at a temperature of 4.2 K (*TEnd*). The neck segment is heated by the radiation heat flux from the surface at a temperature of 77 K (*TRad*). The aim of the calculation was to find the heat fluxes *QN3B* and *QN3E* at both ends of the segment. The input parameters of the neck segment and results of the KRYOM calculation are listed in Table 6. A data file with the dependence of the unit length heat conductivity of the neck (wall + He gas) on the temperature was created in advance and used for the calculation.

Table 6 Parameters of the neck segment L2 from KRYOM

Input parameters	Value	Description
Length [mm]	365	
dx [mm]	0.1	step of calculation (estimated)
TBeg [K]	77	temperature of the upper end
TEnd [K]	4.2	temperature of the lower end
TRad [K]	80	surrounding surface temperature
TolT [K]	0.01	tolerance of the Tend temperature
QL [mW]	0	
EH	0.1	mutually emisivity
KCp	1	(ideal heat exchange)
Results		
QN3B [mW]	13	
QN3E [mW]	18	

Calculated heat fluxes *QN3B* and *QN3E* are nearly the same (Table 6), because heat conductivity of the neck segment is predominant in comparison with the radiation heat flux.

Neck segment of the LHe vessel

The LHe vessel is together with the segment *L5* of the LHe central neck. The LHe vessel is shielded by the LN2 vessel (77 K) with the LHe shield (80 K). The LN2 vessel is thermally connected to the LHe neck. This LN2 thermal anchor divides the LHe neck into two segments. Therefore the temperatures at the upper and lower ends of the neck segment *L5* are supposed to be about 77 K (*TBeg*) and 4.2 K (*TEnd*), respectively. The neck wall is cooled by the He gas evaporating from the LHe vessel and heated by radiation from the surrounding surfaces at a temperature of 77 K (*TRad*).

The filling neck of the heat exchange chamber, which passes through the LHe central neck, must be included into the heat analysis. Hence both necks are taken as one tube. The cross-section of the heat exchange chamber neck was integrated into the cross-section of the LHe neck (inner diameter, wall thickness and neck segment length equal to 47.4 mm, 0.5 mm, 406 mm respectively).

The calculation procedure is the same as in the convection cell tubes analysis but the neck is now cooled by the stream of evaporated He. The heat fluxes *QN5B* and *QN5E* through the neck segments and the heat fluxes *QS4* = *QN5B* – *QN5E* to the LN2 vessel through the thermal anchors can then be evaluated.

Heat flux through the supporting straps

The supporting straps (three elements of 2 mm^2 rectangular cross-section and 90 mm in length) are placed in the vacuum space between the LHe shield and convection cell shield, thus the temperatures of their ends are 80 K and 4.2 K. A heat conductivity of $2 \cdot 10^{-5}$ W/K for all elements was evaluated for the used geometry and material (fibreglass and epoxy resin composite). The heat flux *QC2* through the elements can be consequently evaluated.

4.4.4 Heat flux analysis of the LN2 subsystem

The LN2 system analysis was performed in a similar way as for the LHe system. The results of the heat flux analysis of the LN2 subsystem are summarised in Table 7.

Table 7 The results of the heat flux analysis of the cryostat

Heat transport in the necks	mW	Comments
QN1B (4.2 K)	-1.7	
QN1E (4.2 K)	1.3	
QN2B (4.2 K)	-2.2	
QN2E (4.2 K)	2.4	
QN3B (77 K)	13.2	
QN3E (4.2 K)	17.6	
QN4B (300 K)	380	
QN4E (77 K)	160	
QN5B (77 K)	989	
QN5E (4.2 K)	0.1	
QN6B (300 K)	2778	
QN6E (77 K)	717	
QN7B (TS2 [K])	4758	
QN7E (77 K)	8	
QN8B (300 K)	1256	
QN8E (TS2 [K])	16	
Heat radiation between surfaces	**mW**	
QR2	33	
QR3	5495	
QR4	10347	
Heat conducted in supporting straps	**mW**	
QC2	1.5	for 3 elements
QC3	33	for 3 elements
QC4	0	undefined thermal contact
Radiation shield cooling	**mW**	
QS1	-4	*QN1B-QN2E*
QS2	-20	*QN2B-QN3E*
QS3	-147	*QN3B-QN4E*
QS4	272	*QN5B-QN6E*
QS5	4742	*QN7B-QN8E*
Temperatures of the shields	**K**	
TS1	4.3	
TS2	223	
Distances	**mm**	
L1	140	
L2	215	
L3	365	
L4	220	
L5	406	
L6	165	
L7	110	
L8	50	
Total heat flux into the LHe vessel	**mW**	
QL	60	
Total heat flux into the LN2 vessel	**mW**	
QL	5460	
Consumption of cryoliquids	**litre/day**	
LN2	3.0	
LHe	1.9	

4.4.5 Parasitic heat flux analysis of the convection cell

Parasitic heat fluxes can directly influence the precision of the experiment. The analysis of the parasitic heat fluxes was done with respect to the regimes of the convection experiment. For the calculation of the total parasitic heat flux to the convection cell the following sources must be taken into account:

- Heat flux *QN1* through the segment *L1* of the convection cell tubes
- Heat flux *QT1* through the filling tube that connects the LHe vessel to the convection cell
- Radiation heat flux *QR1* between the LHe shield and the cell
- Heat flux through the current leads of the resistance heaters in the Cu plates together with the Joule heat due to the current *QH1*

Convection cell tubes

The heat fluxes *QN1* through the segments *L1* of the convection cell tubes into the convection cell were calculated. The tube segment *L1* is loaded by the radiative heat flux from the LHe shield at a temperature of 80 K. The upper end of the *L1* segment is connected by the thermal anchor to the LHe vessel at temperature of 4.2 K. The heat fluxes *QN1* into the cell were evaluated for several mean temperatures *T* of the cell (Table 8). The temperatures of the cell vary from 4.5 K to 12 K.

Convection cell filling tube

The heat fluxes *QT1* through the filling tube between the LHe vessel (4.2 K) and convection cell (4.5 K – 12 K) were calculated (Table 8). The filling tube is made of copper and stainless steel tubes. The second one serves as thermal resistance for the heat flux to the cell.

Current leads

The resistance heater of the bottom copper plate of the convection cell is powered by two copper current leads of 0.15 mm in diameter and 200 mm in length. The current leads are thermally anchored to the cell shield (4.3 K) and to the bottom of the cell, which has a varying temperature (4.5 K – 12 K). Heat fluxes through the current leads *QH1* were calculated by the VVV_2 software [40]. The programme computes temperature and heat flux profiles along the length of a conducting wire situated in vacuum. The Joule heat generated in the wire and radiated to the surroundings is taken into account. Results of the calculations are shown in Table 8.

Convection cell shield

The shield is made of copper of RRR = 40 and of 1 mm wall thickness. The cell shield is thermally connected to the bottom of the LHe vessel (4.2 K) where ideal thermal contact is assumed. The shield is heated by radiation heat flux from the LHe shield at a temperature of 80 K. The 4.3 K maximal temperature of the bottom shield was calculated. The radiation heat fluxes *QR1* between the cell shield at the calculated temperature 4.3 K and the convection cell at temperatures in the range from 4.2 K to 12 K were also calculated (Table 8).

Discussion of the parasitic heat flux results

The results of the parasitic heat flux calculations are summarized in Table 8 and plotted in Figure 18. The tubes heat fluxes *QN1*, *QT1* flow to the middle part of the cell

and can be counted up (*QTubes*). The heat flux *QH1* flows to the bottom plate of the convection cell and directly influences the measured convection heat flux. It is possible to neglect the radiation heat flux *QR1*.

Table 8 Parasitic heat fluxes to the convection cell

Tcell	QN1	QT1	QH1	QR1	QTubes
K	mW	mW	mW	mW	mW
4.5	0.22	-0.01	0.00	0.00	0.21
5	0.18	-0.02	0.03	0.00	0.16
6	0.12	-0.10	-0.09	0.00	0.02
8	-0.02	-0.20	-0.24	-0.01	-0.22
10	-0.22	-0.30	-0.40	-0.01	-0.52
12	-0.48	-0.50	-0.66	-0.03	-0.98
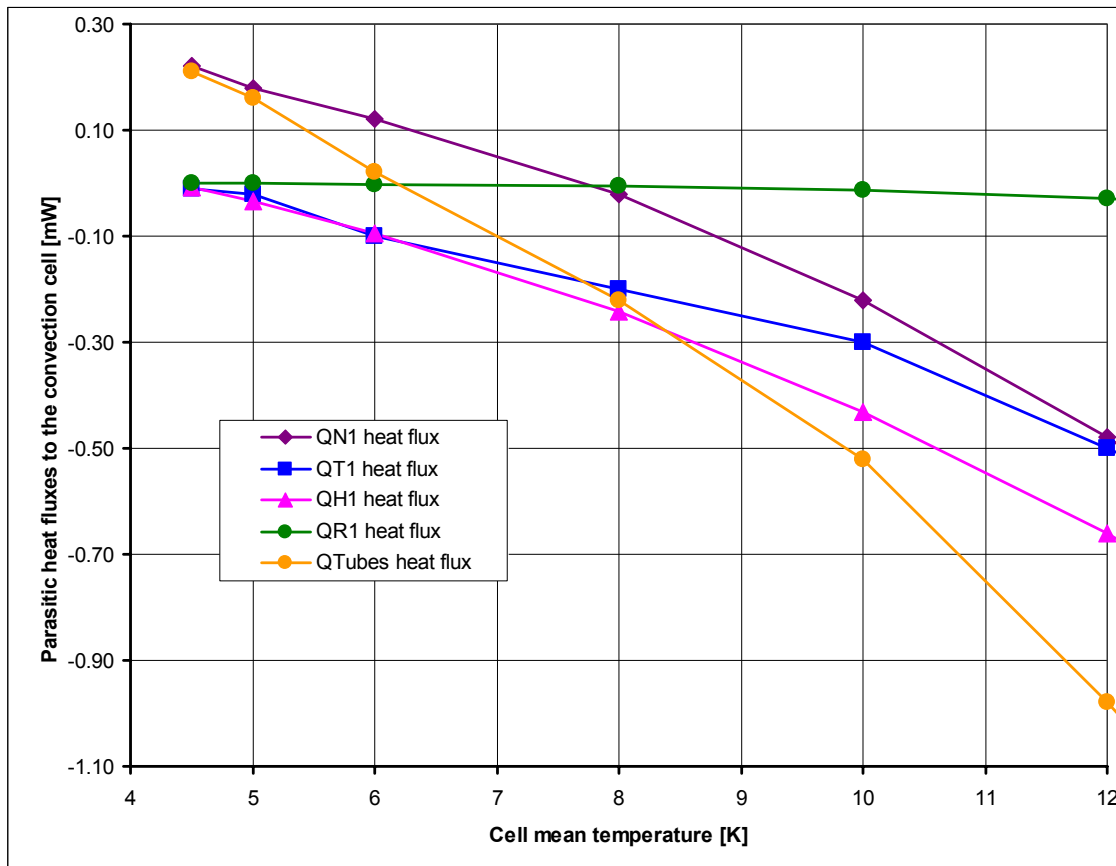
Figure 18   Parasitic heat fluxes to the convection cell

4.5   Delimitation of applicable convection heat fluxes

The convection heat fluxes for the convection experiment are delimitated by:

- Heat conductivity of the heat exchange chamber (maximum)
- Parasitic heat fluxes (minimum)

The convection heat fluxes used in experiment and predicted in sec. 3.5.1 (Figure 11) are plotted in Figure 19. The maximum heat flux *QCH* which can be transferred via the

heat exchange chamber (blue line) represents the highest value of the convection heat flux useable in the experiment. The heat flux *QCH* is evaluated under the condition that the heat exchange chamber operates between 4.2 K and T_t (i.e. the temperature of the cell top plate). In fact, this flux is limited by the condensation of He gas in the heat exchange chamber.
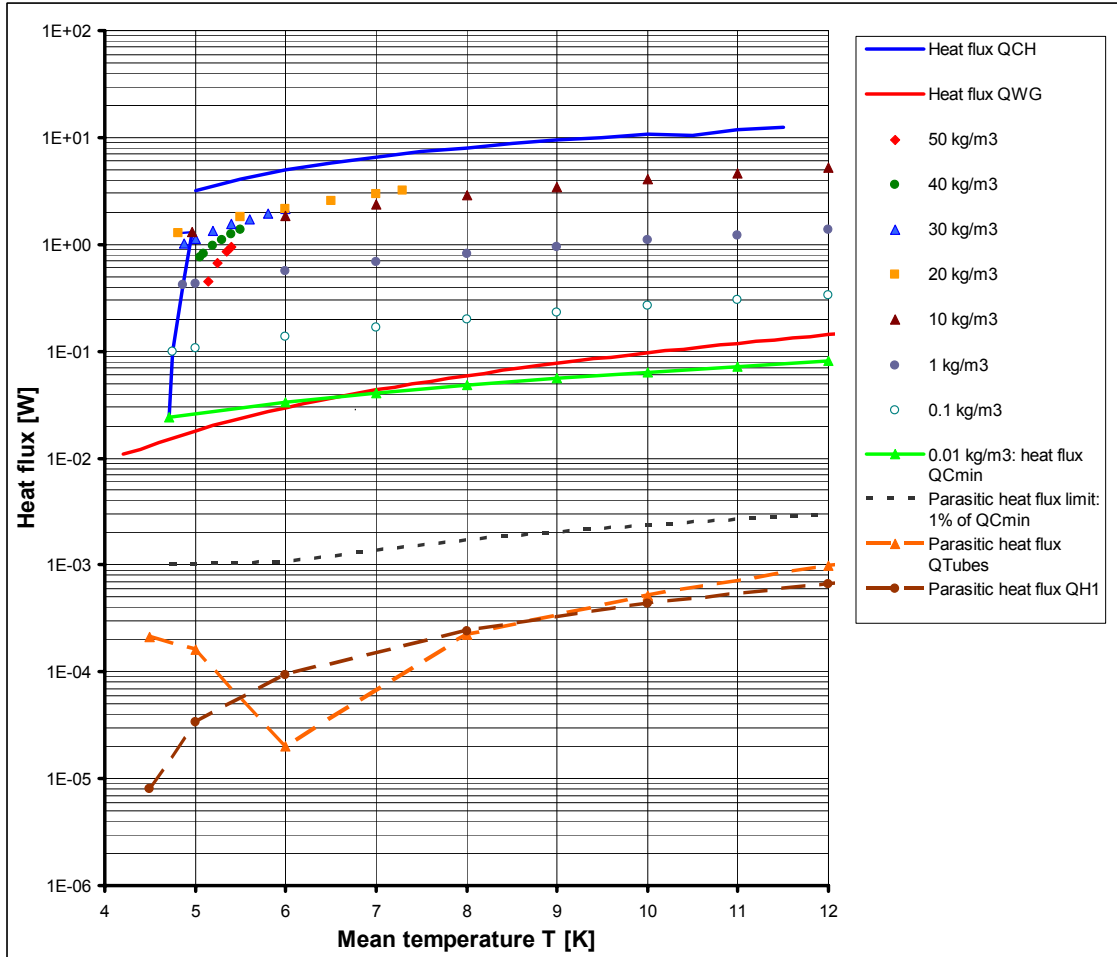
Figure 19   Dependence of the cell heat fluxes on the mean temperature T.

QCH – the maximum heat flux which can be transferred via the heat exchange chamber
QWG – the minimum heat flux via the heat exchange chamber
Coloured spots – the area of the convective heat fluxes used in experiment and predicted in sec. 3.5 (Figure 11)
QCmin – the lowest convective heat flux that represents the minimum heat flux used in experiment
Parasitic heat flux limit – represents the 1 % of QCmin
QTubes – the heat fluxes through the tubes of the cell
QH1 – the heat fluxes through the current leads

To reach the temperature of the upper plate of the heat exchange chamber as low as possible, the heat conductivity of this plate is to be very high. In case of a stainless steel bottom plate, which would be easier to produce, the thermal resistance of the plate would decrease the heat conductivity of the chamber and thus limit the highest measurable *Ra*, *Nu* numbers and increase the LHe consumption (Figure 20(a-b)). Therefore the bottom of the LHe vessel is made of copper (Figure 13).

The minimum heat flux through the heat exchange chamber is given by the heat conduction flux QW in the chamber wall and by the conduction flux QG of the He gas at lowest achievable pressure. The flux QWG (red line in Figure 19) was calculated as the sum of the both fluxes, if the wall is of 1 mm in thickness and of 50 mm in height and the pressure is equal to 0.1 Pa.

Absolute values of the parasitic heat fluxes to the convection cell are shown in Figure 19. These fluxes are lower than 1 % of the lowest convective heat fluxes $QCmin$ at density 0.01 kg/m^3 of He in the cell. It means that in experiment with the density higher than 0.01 kg/m^3 parasitic heat fluxes are negligible.
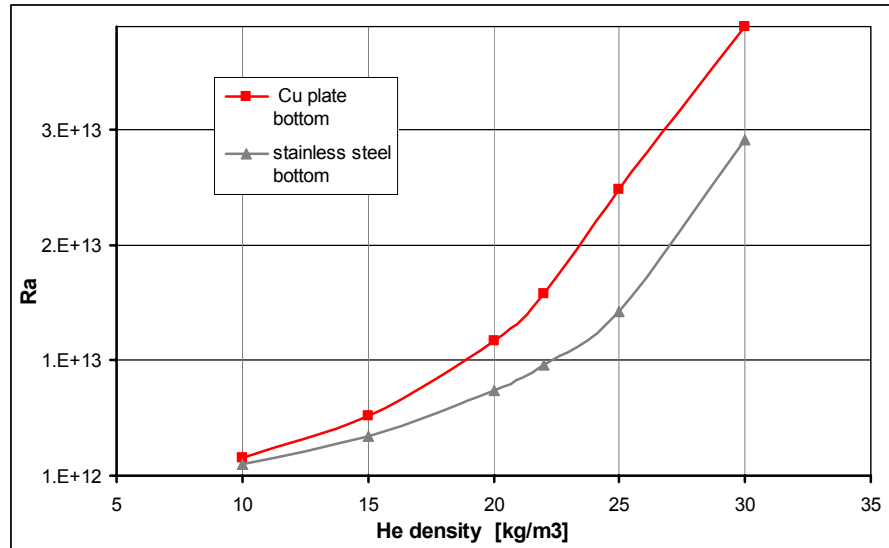
Figure 20   (a) Influence of the bottom plate material of the LHe vessel on the Ra values that can be achieved in the experiment under the Boussinesq condition $\alpha \cdot \Delta T = 0.2$)
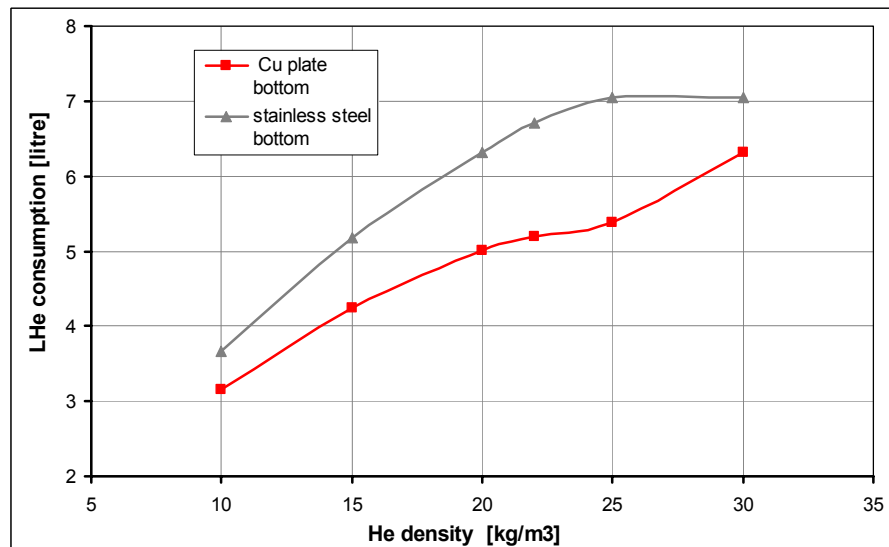
Figure 20   (b) Corresponding LHe consumption. Estimated for a bottom plate thicknesses of 10 mm (copper) and 5 mm (stainless steel).

4.6 Helium control system of the cryostat

The helium control system of the cryostat is schematically presented in (Figure 21). The components of the helium control system are described in Appendix 2. This system is composed of four lines (A, B, C and D). Line A serves for the LHe filling of the cell and is provided with a safety valve with a bursting disc and reserve pressure gauge. Line B is used to empty the cell by the means of the vacuum pump connected to the He recovery system and is provided with a safety spring valve and pressure gauge. Line C connects the heat exchange chamber to the pure GHe pressure vessel and vacuum pump and is equipped with a safety spring valve and pressure gauge. Line D, provided with two spring safety valves, serves for the filling of the LHe vessel and connects the LHe vessel to the He recovery system.
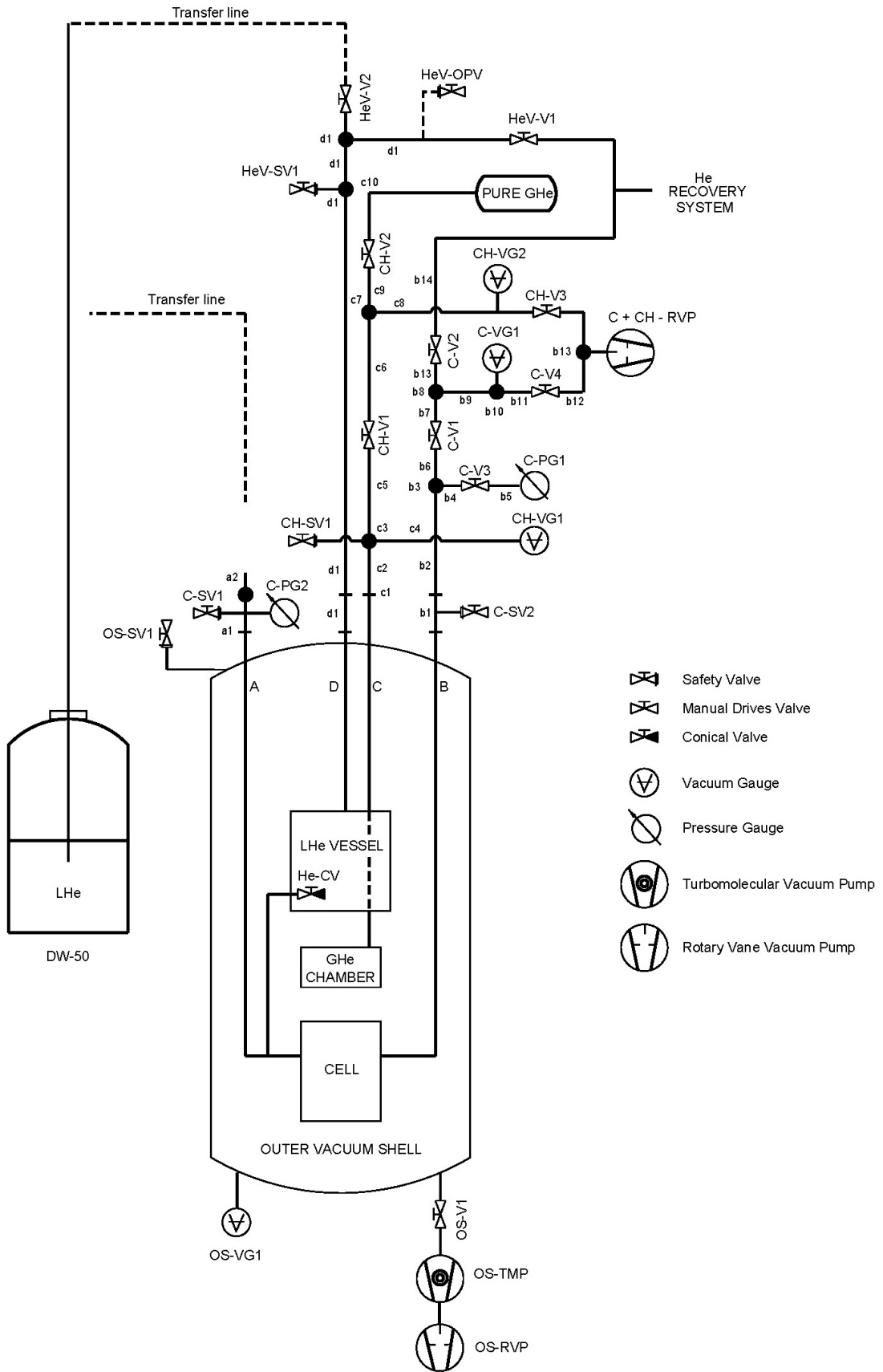
Figure 21   Helium control system of the cryostat

4.7   Operation safety

The following model was considered to account for possible hazards.

The supercritical He is in quasi-equilibrium state in the convection cell. The vacuum insulation space is suddenly filled with He gas and is a cause of the heat load on the convection cell. Natural convection develops in the vacuum insulation space. At the maximum pressure a steady-state adiabatic flow of He (single-phase and subsonic) through a vent line is supposed. The heat load was estimated by using the heat transfer formula for natural convection in the gas between concentric spheres [34]. The cryostat with the cell was approximated by 5 concentric spheres filled with 1 bar He gas (the outer shell at 300 K, the three shields at temperatures maintained by the developed convection and the cell at about 5 K). As a result a maximum heat load of about 1000 W was obtained.

At a given heat load to a vented cell, the highest pressure in the cell develops for He density of about 50 kg/m^3. The corresponding mass flow dm/dt = (0.06 ± 0.01) kg/s is released at the maximum pressure inside the cell. The value of the maximum pressure depends on the hydrodynamic resistance of the vent line and corresponding relief valves (e.g. a spring valve and bursting disk). Along the vent line of 15 mm in diameter and 1 m in length a pressure drop of 28 kPa develops. The vent line is equipped with pressure safety valves (Appendix 2) and can safely release a mass flows generated by heat loads up to 2000 W at a pressure in the cell lower than the test-pressure 350 kPa.

4.8   Time schedule of experiments

The preparation of a "warm" cryogenic apparatus for experiments needs a minimum time. Cooling the apparatus down includes in fact several consecutive steps: evacuation of the cryostat, evacuation of the experimental cell, cooling by LN2, filling the LHe vessel with LHe, filling the exchange vessel with He gas and filling the experimental cell with He. These steps require together 1-2 weeks. The thermal stabilization of the whole system can take a few days depending on the required measurement precision.

For one filling of the cell (one value of He density), values of *Ra* within a range of about one and a half order of magnitude can be measured. For example, the measurement of seven points for the *Nu*(*Ra*) dependence (*Ra* from 10^{13} to 10^{12}, He density of 30 kg/m^3) takes about 20 hours (time for stabilization and measurement). The consumption of LHe is 55 litres in this case (Appendix 1).

5 Realization of the cryostat

5.1 The convection cell

5.1.1 Materials and technology of joints

A prototype of the bottom part (Figure 13, Figure 15) of the convection cell was initially manufactured to check the joint technology (i.e. quality of indium sealing, brazing and welding) at room and cryogenic temperatures. Some material and technological problems were found.

The flanges and rings

The flanges and rings were manufactured from stainless steel sheets AISI 304 (DIN 1.4301). Several cracks were detected in the stainless steel ring and flanges in the region thermally affected by the welding [30]. An analysis of the cracks in the stainless steel was made at the Institute of Material Science of the Technical University in Brno.

The analysis revealed that the cracks were created along the δ-ferrite particles by welding stresses (thermal expansions) after plasma welding. Present impurities probably also contributed to this effect.

The problem was discussed in detail with PBS Velká Bíteš, producer of turbines for the LHe liquefiers, and it was concluded that the impurities in the flanges material were the causes of the cracks and that this material imperfection was generated during the production of the steel sheets.

Another difficulty appeared in connection with vacuum brazing of the copper plate to the stainless steel ring. The brazing is realized in a vacuum furnace by using an Ag (78 %) eutectic brazing solder. The poor weldability of the stainless steel surface with the used brazing solder affected negatively the vacuum tightness and mechanical strength of this joint.

From three types of stainless steel sheets of good weldability (made of AISI 304, 304 L and 316) 28 samples were prepared to be tested with vacuum brazing with the copper. On these samples various procedures of cleaning (washing, electrolytic etching), surfaces treatment (nickel plating) and heating time sequences in the vacuum furnace were tested.

As a result the stainless steel AISI 304 L (DIN 1.4307) was chosen. Within these tests a new procedure for vacuum brazing was elaborated (Appendix 3).

Copper plates

OFHC copper plates were purchased from the Finland Outocumpu company, producer of superconducting wires. The vacuum tightness of the plates was tested by a He leak detector.

Once ready the plates were annealed in the vacuum furnace at 650 °C.

The heat conductivity of these plates was determined by measuring the RRR (Residual Resistance Ratio). Sample for the measurement was cut off from the copper plates during lathe-turning and annealed together with the plates. For the annealed sample the value of RRR = 290 was found. The heat conductivity of 1800 W/m/K (4.2 K) was determined from this RRR value.

5.1.2 Realization of the convection cell parts

The bottom and middle parts of the cell can be seen in Figure 22. The internal side of the bottom part is shown in Figure 22(a). The copper plate is machined by soft lathe-turning and the surface roughness is not larger than $R_a = 1.6$ µm. The groove is milled on the external side Figure 22(b) for a resistance heater and two holes are drilled here for temperature sensors in the centre and at the margin of the copper plate. The middle part with parts of the filler necks and the top part of the cell with the lower part of the heat exchange chamber are shown in Figure 22(c-d).
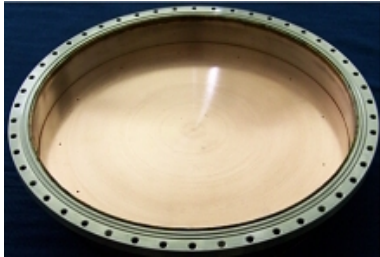
a) Bottom part - internal side view
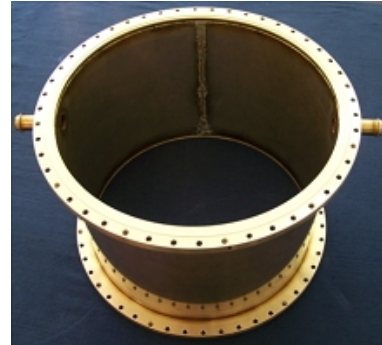
c) Middle part
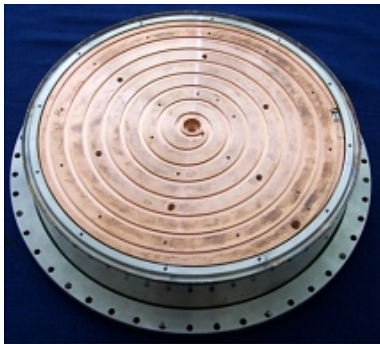
b) Bottom part - external side view

d) Top part of the cell

Figure 22   Parts of the convection cell

5.1.3 Testing of the convection cell

By using the developed technology, the bottom and top parts were manufactured. Several successful tests at room and LHe temperatures were done in the testing cryostat HKP (Figure 23) up to an overpressure of 350 kPa. Helium gas was used as the testing medium. The tightness of both parts was checked at the test pressure via a He leak detector.

The middle part of the cell was tested at room temperature by using water as testing fluid. The testing pressure was 350 kPa.
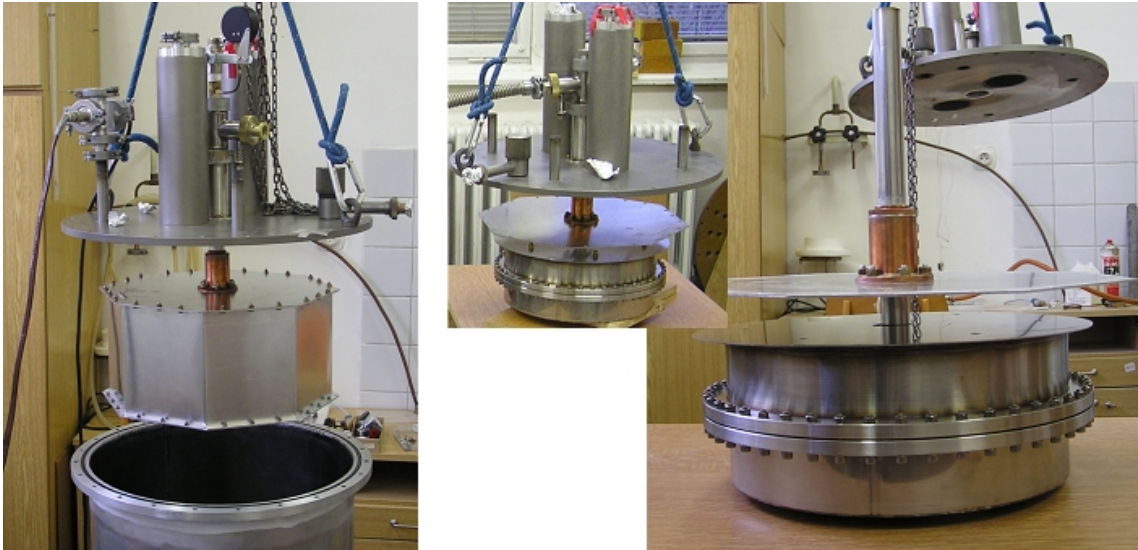
Figure 23   Testing of the bottom part of the cell in the test cryostat HKP

5.1.4   Convection cell assembly

The assembly of the whole convection cell is illustrated in Figure 24, where the convection cell is composed of the bottom, middle and the top parts.

Top part with the portion of the heat exchange chamber

Exchangeable central part

Bottom part

Assembling plate
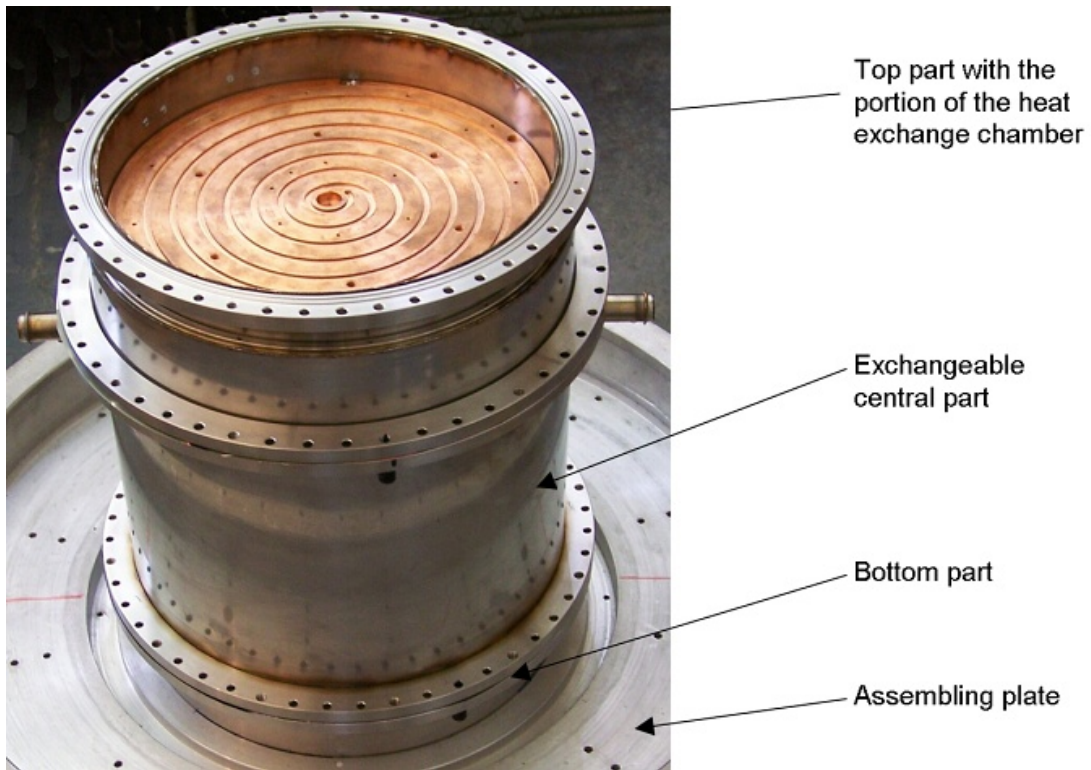
Figure 24   Assembly of the convection cell

5.2 LHe vessel assembly

Assembly of the LHe vessel with a filling neck (central neck of the cryostat) is shown in Figure 25(a). The LHe vessel is made of stainless steel with exception of the bottom middle plate which is made of copper (Figure 25(b)).

d) LHe valve

b) View inside the LHe vessel

a) Assembly of the LHe vessel

c) Bottom part of the LHe vessel, top part of the heat exchange chamber
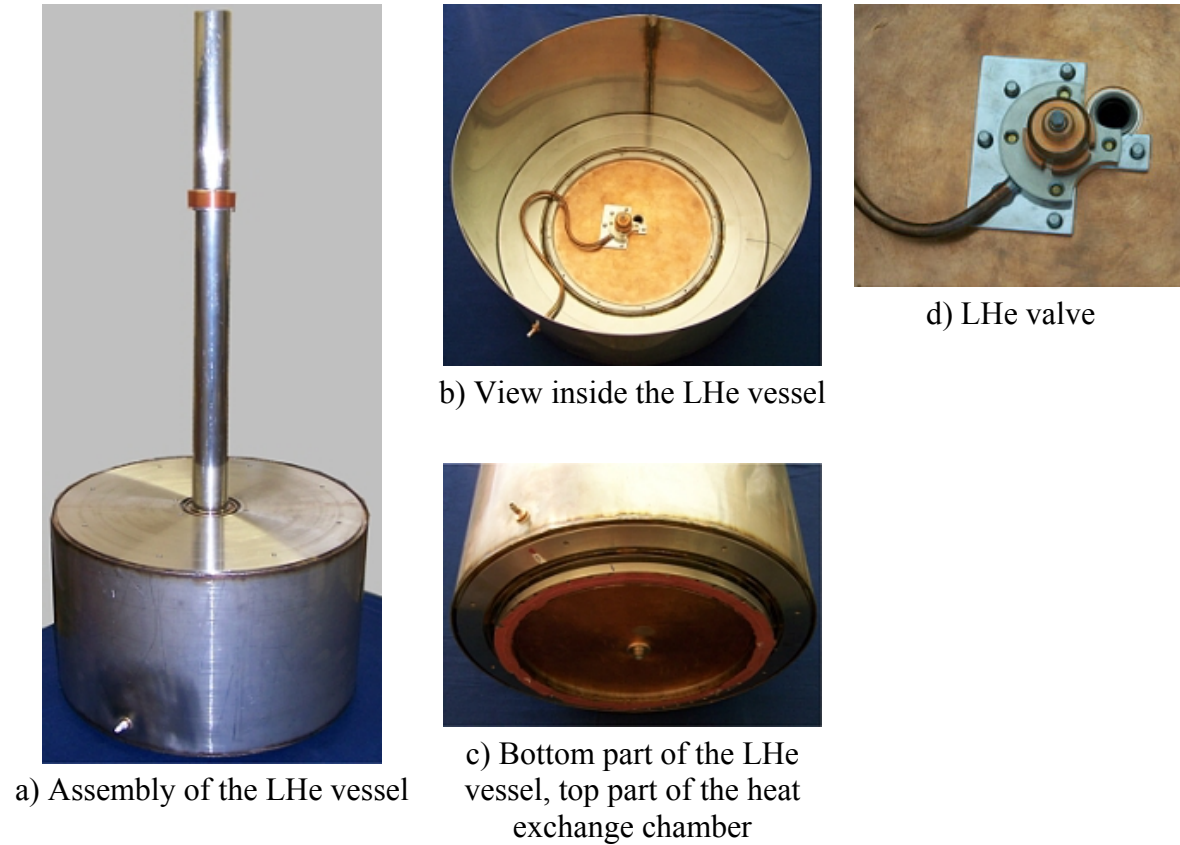
Figure 25   Assembly and parts of the LHe vessel

The copper bottom part transfers the heat flux from the heat exchange chamber to the liquid in the LHe vessel. The upper portion of the heat exchange chamber, which is a part of the LHe vessel, is shown in Figure 25(c). The stainless steel bushing is vacuum brazed to the copper bottom part.

A liquid He valve is placed on the copper bottom part in the LHe vessel (Figure 25(b and d)). The convection cell will be filled by this valve during experiments. The valve is connected to the cell by a copper tube that passes through the cylindrical walls of the LHe vessel and the cell middle part. The liquid He valve was specially designed and manufactured for this cryostat.

5.3   Cryostat assembly

In Figure 26 the complete cryostat and the experimental cell in the dismantled cryostat are shown.

Figure 26   Cryostat assembly

6 Perspectives of the convection experiments

The experimental work with the cryostat will proceed within the project GAAV [35] which is aimed at the following problems:

Kraichnan regime

The study of the transition to the Kraichnan regime and corresponding measurement of the $Nu(Ra)$ dependence within the range of Ra numbers $10^8 - 10^{14}$ (10^{15}) will be done for various He states.

The obtained results will be analysed taking into account the available theoretical models and experimental data from other laboratories.

Prandtl number effect

The influence of the Pr number on the $Nu(Ra)$ dependence near the He critical point will be tested.

Structures of the flow inside the cell

The large-scale circulation (sec. 1.3.2) inside the cell will be investigated at several positions in the experimental cell by detailed measurements of the temperature and velocity time dependence.

The cell design also enables to change the aspect ratio. Additional measurement with modified cells (e.g. different aspect ratio Γ and location of temperature sensors) can then be performed.

Convection in constricted cell

A completely new feature of the cell design gives the opportunity to change its geometry and thus perform experiments complementary to the studies on thermally driven quantum turbulence. A close similarity in the heat transport efficiency has been already pointed out [36]. The convection will then be observed in this constricted middle part.

Collaboration

The experimental data will be interpreted in collaboration with prof. L. Skrbek, head of the Department of Low Temperature Physics, Faculty of Mathematics and Physics, Charles University, and with prof. J. J. Niemela, deputy director of the ICTP Trieste, the coauthors of publication [14]. The group headed by prof. Skrbek deals with complementary research on turbulence in He superfluid.

7 Discussion

As it is not possible to realize an ideal convection cell, the result of experiment is potentially influenced by heat conductivity and capacity of the cell envelope (sidewalls and plates) and by parasitic heat fluxes into the cell. In this section we discuss the effects that could influence observed convection in the designed cell in comparison with the cells of other laboratories.

At the high Ra numbers, contradictory results on the scaling law $Nu(Ra)$ of convection in cold He were published. While Niemela et al. obtained scaling law with exponent of about 1/3 in the cells with aspect ratio Γ = 1/2, 1 and 4 [14], [10], [22], "transition to the scaling law with exponent 1/2" was observed by Grenoble group in various cells characterized by Γ = 1/2 [17], [18], [19].

Generally, the Nu number depends both on the Ra and Pr numbers. The domain of Ra and Pr points representing experiments of Niemela et al. (Γ = 1, L = 0.5m) and of Grenoble group (Γ = 1/2, L = 0.2 m) are very near to the domain of Ra, Pr in the experiment planed for the designed convection cell. Thus the scaling law $Nu(Ra)$ in those three experiments is possible to be measured at nearly the same values of Pr number.

Geometrical and material parameters of the convection cells of those three experiments are summarized in Table 9 and briefly discussed in the following paragraphs.

Table 9 Parameters of the cells used in discussed experiments

Laboratory	Grenoble	Oregon (Niemela et al.)	ISI (Brno)
Aspect ratio Γ	1/2	1	1
Cell height L [m]	0.2	0.5	0.3
Wall thickness t [mm]	0.50	3.0	0.50
Thermal contact between sidewall and plate	weak	direct	weak
Wall number W	0.48	0.58	0.16
Plates	OFHC	OFHC	OFHC
Plates thickness a [mm]	25	38	28
Plates roughness [micrometers]	Smooth and 100	10	1.6
Heat conductivity of plates at 5 K λ_p [W/m/K]	1200	~1000	2100
$a.\lambda_p$ [W/K]	25	38	50

Sidewall effect

The designed cell with thin-sidewall (thickness of 0.5 mm) is characterised by very low wall number W = 0.16 (see sec. 1.3.5). For a comparison with other cells see Table 9.

By using the formula of Roche et al. [27], we can estimate that the corrections for Nu numbers eliminating sidewall effect are equal to about 2 % at $Ra = 10^{12}$ and 10 % at $Ra = 10^8$. These values are much lower than those for similar cells of other laboratories (see sec. 1.3.5).

In addition to the small thickness, the sidewalls are in very weak thermal contact with the copper plates (Figure 13) which further reduces the undesirable effect of the heat flowing directly from the plates in the sidewalls.

Copper plates

At high Rayleigh numbers the heat conductivity of the copper plates can influence the convection inside the cell (see sec. 1.3.6). The criterion *Cr* for possible convection restrictions due to the plates is evaluated for the designed cell (Brno) in comparison with the cells of the laboratories in Grenoble and Oregon (Figure 27). According to the analysis in sec. 1.3.6., the convection is potentially restricted by conductivity of plates at about *Cr* < 1. This occurs at *Ra* numbers higher than 10^{12} (Figure 27). From the point of view of this criterion the designed cell is comparable with the Grenoble cell that provides the highest values of *Cr*. The Grenoble group used in fact the plates of conductivity 240·*T* [W/m/K] that is smaller than that of the plates used by us, i.e. 420·*T* [W/m/K]. The value of the criterion Cr decreases with increasing dimension of the cell and increases in proportion with the product of heat conductivity and thickness of plates. This product is the highest in the ISI cell among the cells presented in Table 9.
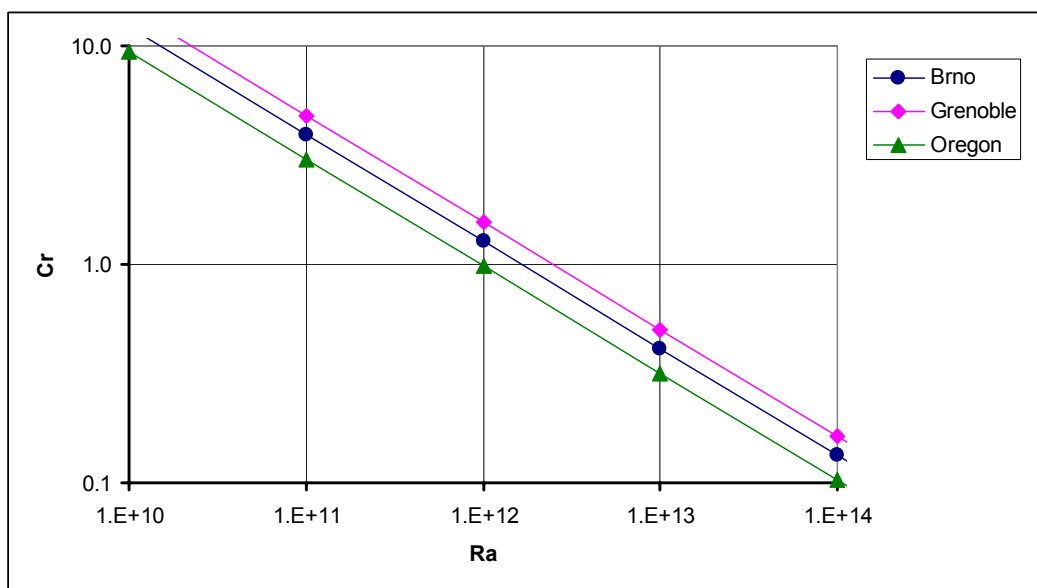
Figure 27   Criterion for convection restriction due to the copper plates Cr in dependence on the Rayleigh number Ra

Parasitic heat fluxes

The parasitic heat fluxes into the convection cell were minimized up to a value of 1 mW (sec. 4.4.5). Such a low value enables us to measure values of *Nu* number down to at least 20 (*Ra* ~ 10^7). At the measurement of *Nu* = 20 the parasitic heat fluxes are less than 1 % of the convective heat flux.

8 Conclusions

A helium cryostat with the cylindrical convection cell, 300 mm in both diameter and height, has been designed, manufactured, assembled and tested. The whole apparatus is ready for experiments on very high Rayleigh number turbulent convection, using cryogenic helium gas as a working fluid. The cell is designed for the experiment which ought to resolve the existing contradictions in various aspects of the convective flow and heat transport, especially in the scaling exponent of the $Nu(Ra)$ power law dependence (sec. 1.3.4), with the advantage of the so far minimal influence of the cell structure on the convection at both low and high ends of the attainable range of Ra numbers.

To achieve this goal, the convection cell was designed with especially thin sidewalls of as low as possible parasitic heat conductivity. The thin sidewall together with careful minimization of other parasitic heat fluxes reduces undesirable effects on the observed convection in the region of lower Ra values (sec. 4.4.5 and sec. 7). On the other hand, the use of the thick best available quality high-conductivity OFHC copper plates making the top and the bottom of the cell and additional annealing of them before installation minimizes any restrictive influence of the plates on convection at the upper end of attainable Ra (sec. 1.3.6 and sec. 7).

Expected accuracy for the planned experiments has been evaluated based on:

- availability of commercially calibrated highly sensitive and stable Lake Shore Ge temperature sensors together with the ones additionally re-calibrated to increase the accuracy of measured temperature difference between plates

- high-precision Baratron pressure sensor calibrated (traceable to NIST standards) up to 500 kPa and corresponding read-out electronics

- cryogenic Lake Shore 340 temperature controller

The $Nu \sim Ra^{\gamma}$ scaling law for $20 < Nu < 4000$ can be measured with precision better than 7% for each individual point (uncertainty with covering probability 95%). We emphasize that the range $10^7 < Ra < 4 \cdot 10^{14}$ which corresponds to these Nu under assumption of γ near to 1/3 is sufficient to resolve the published controversies on the $Nu(Ra)$ scaling law (sec. 1.3.4).

This work has been conducted at the Institute of Scientific Instruments of the ASCR, v.v.i., Group of Cryogenics and Superconductivity.

The existence of the developed experimental equipment allowed the author of this publication to apply for the research project at GAAV [35] that ought to resolve the objectives listed in sec. 6. This project has already been granted and is scheduled for 2009 - 2011.

9 References

[1]   TRITTON, D. J. Physical fluid dynamics. 2nd edition. Oxford : Clarendon Press, 1988. – ISBN 0198544898.

[2]   SOMMERIA, J. The elusive 'ultimate state' of thermal convection. Nature, 1999, n. 398, pp. 294-295. – ISSN 0028-0836.

[3]   KRAICHNAN, R. H. Mixing-length analysis of turbulent thermal convection at arbitrary Prandtl number. Physics of fluids, 5, 1962, pp. 1374.- ISSN 0899-8213.

[4]   VERZICCO, R. ; SREENIVASAN, K. R. A comparison of turbulent thermal convection between conditions of constant temperature and constant heat flux. Journal of fluid mechanics, 2008, 595, pp. 203-219. – ISSN 0022-1120.

[5]   ROCHE, P. E. ; GAUTHIER, F. ; CHABAUD, B. ; HÉBRAL, B. Ultimate regime of convection : robustness to poor thermal reservoirs. Physics of fluids, 14, 2005, pp. 115107/1-4. – ISSN 0899-8213.

[6]   LOHSE D. ; TOSCHI, F. Ultimate state of thermal convection. Physical review letters, 90, 2003, no. 3, pp. 034502/1-3. ISSN 0031-9007.

[7]   KADONOFF, L. P. Turbulent heat flow. Physics today, 54, 2001, pp. 34-39. – ISSN 0031-9228.

[8]   NIEMELA J.J. ; SREENIVASAN K. R. Formation of the"Superconducting" Core in Turbulent Thermal Convection. Physical Review Letters 100, 2008, Art. No. 184502. ISSN 0031-9007.

[9]   AMATI G ; KOAL K ; MASSAIOLI F ; SREEVANASAN K.R. ; VERZICCO R. Turbulent thermal convection at high Rayleigh numbers for Boussinesq fluid of constant Prandtl number. Physics of Fluids 17, 2005, 121701.- ISSN 0899-8213.

[10]   NIEMELA, J. J. ; SREENIVASAN, K. R. Confined turbulent convection, Journal of fluid mechanics, 2003, 481, pp. 355-384. – ISSN 0022-1120.

[11]   NIEMELA, J. J. ; SKRBEK, L. ; SREENIVASAN, K. R. ; DONNELLY, R. J. The wind in confined thermal convection. Journal of fluid mechanics, 2001, 449, pp. 169-178. – ISSN 0022-1120.

[12]   NIEMELA, J. J. ; SREENIVASAN, K. R. The use of cryogenic helium for classical turbulence: promises and hurdles. Journal of low Temperature physics, 143, 2006, n. 5-6, pp. 163-212. – ISSN 0022-2291.

[13]   SKRBEK, L. ; NIEMELA, J. J. ; DONNELLY, R J. Turbulent flows at cryogenic temperatures : a new frontier. Journal of physics : condensed matter, 11, 1999, pp. 7761-7782. – ISSN 0953-8984.

[14]   NIEMELA, J. J. ; SKRBEK, L. ; SREENIVASAN, K. R. ; DONNELLY, R. J. Turbulent convection at very high Rayleigh numbers. Nature, 2000, n. 404, pp. 837-840. – ISSN 0028-0836.

[15]   ASHKENAZI, S. ; STEINBERG, V. High Rayleigh number turbulent convection in a gas near the gas-liquid critical point. Physics review letters, 83, 1999, pp. 3641 – 3644. – ISSN 0031-9007.

[16]   NIST Reference Fluid Thermodynamic and Transport Properties Database (REFPROP), Version 8.0, National Institute of Standards and Technology, USA (2000).

[17]   CHAVANNE, X. ; CHILLA, F. ; CHABAUD, B. ; CASTAING, B. ; CHAUSSY, J. ; HEBRAL, B. High Rayleigh number convection with gaseous helium at low

temperatures. Journal of low temperature physics, 1996, vol. 104, n°1-2, pp. 109-129. – ISSN 0022-2291.

[18] CHAVANNE X. ; CHILLA F. ; CASTAING B. ; HÉBRAL B. ; CHABAUD, B. ; CHAUSSY, J. Observation of the ultimate regime in Rayleigh-Bénard Convection. Physical review letters, 79, 1997, n. 19., pp. 3648-3651. – ISSN 0031-9007.

[19] CHAVANNE X. ; CHILLA F. ; CHABAUD B. ; CASATING B. ; HEBRAL B. Turbulent Rayleigh- Bénard convection in gaseous and liquid He. Physics of fluids, 13 2001, n. 5, pp. 1300-1320. – ISSN 0899-8213.

[20] GAUTHIER F. ; ROCHE P. E. Evidence of a boundary layer instability at very high Rayleigh number, EPL 83, 2008, 24005-p1-p6.

[21] GAUTHIER F. ; SALORT, J. ; BOURGEOIS O. ; GARDEN J. L. ; DU PUITS R. ; THESS A. ; ROCHE P. E. Transition on local temperature fluctuations in highly turbulent convection. EPL 87, 2009, 4406.

[22] NIEMELA J. J. ; SREENIVASAN K. R. Turbulent convection at high Rayleigh numbers and aspect ratio 4. Journal of fluid mechanics, 2006, 557, pp. 411-422. – ISSN 0022-1120.

[23] CALZAVARINI, E. ; LOHSE, D. ; TOSCHI, F. ; TRIPICCIONE, R. Rayleigh and Prandtl number scaling in the bulk of Rayleigh – Bénard turbulence. Physics of fluids, 17, 2005, n. 5, pp. 055107/1-7. – ISSN 0899-8213.

[24] KUNNEN R. P. J. et al. Numerical and experimental investigation of structure/function scaling in turbulent Rayleigh-Bénard convection. Physical review, E 77, 2008, pp. 016302/1-13. – ISSN 1539-3755.

[25] AHLERS, G. Effect of sidewall conductance on heat-transport measurements for turbulent Rayleigh-Bérnard convection, Physical review, E 63, 2001, n. 2, pp. 145-154. – ISSN 1539-3755.

[26] CHILLA F, RASTELLO M, CHAUMAT S, CASTAING B. Ultimate regime in Rayleigh-Bénard convection: The role of plates. Physics of fluids, 16, 2004, pp. 2452-2456.- ISSN 0899-8213.

[27] ROCHE P. E. ; CASTAING B. ; CHABAUD B. ; HEBRAL B. ; SOMMERIA, J. Side wall effects in Rayleigh Bénard experiments. European Physical Journal, B 24, 2001, n. 3, pp. 405-408. – ISSN 1434-6028

[28] HANZELKA P. He kryostat NMR-III pro supravodivý magnet spektrometru NMR. In: Sborník přednášek VIII. školy fyziky a techniky nízkých teplot, Vysočina-Sykovec (ÚPT AV Brno), 1988, s. 44 – 45.

[29] MUSILOVÁ V. ; HANZELKA P. ; KRÁLÍK T. ; SRNKA A. Low temperature radiative properties of materials used in cryogenics. Cryogenics, 2005, vol. 45, no. 8, s. 529-536. ISSN 0011-2275.

[30] SRNKA A. ; HANZELKA P. ; MUSILOVÁ V. ; URBAN P. ; SKRBEK L. Design of a Helium cryostat for the study of turbulent thermal convection at cryogenic temperatures. In *Proceedings of the 21st International Cryogenic Engineering Conference : CryoPrague 2006.* Praha : Icaris, 2006 pp. 661-664. – ISBN 978-80-239-8883-3.

[31] URBAN P. ; HANZELKA P. ; MUSILOVÁ V. ; SRNKA A. ; SKRBEK L. Design and tests of the cryostat with an experimental cell for turbulent thermal convection. *Proceedings of the Colloquium Fluid Dynamics 2007.* Praha: Institute of thermomechanics ASCR, 2007, pp. 93-94. – ISBN 978-80-87012-07-9.

[32] Czech technical standard ČSN 69 0010, Stationary Pressure Vessels, (in Czech).

[33] HANZELKA P. Numerical modelling in cryostat design: methods and experimental verification. Cryogenics 1993, 33(4):454-8.

[34] BARRON R. F. *Cryogenic heat transfer*. Philadelphia : Taylor and Francis, 1999. 374 s. ISBN 1-56032-551-8.

[35] Project: Elucidation of fundamental questions in turbulent convection, supported by grant agency GAAV, KJB200650902.

[36] SKRBEK L. ; GORDEYEV A. V. ; SOUKUP F. Decay of counterflow He II turbulence in a finite channel: Possibility of missing links between classical and quantum turbulence. Physical review : E 67, 2003, n. 4, pp. 047302/1-5. − ISSN 1539-3755.

Software

[37] SimRBC, Microsoft Excel Workbook created at ISI AS CR, Group of Cryogenics and Superconductivity.

[38] KRYOM 3.3, created at ISI AS CR, Group of Cryogenics and Superconductivity.

[39] HEPAK, Thermophysical properties of Helium from 0.8 K or the Melting Line to 1500 K, Version 3.40 − Excel Add-In and Version 3.41 − ActiveX DLL, developed by Cryodata, Inc.

[40] VVV_2, created at ISI AS CR, Group of Cryogenics and Superconductivity.

10 Abbreviations and symbols

C_p	$\text{J·kg}^{-1}\text{·K}^{-1}$	Specific heat of fluid at constant pressure
D	m	Diameter of the convection cell
g	kg·m·s^{-2}	Gravity acceleration
H	W·m^{-2}	Heat flux density transferred by natural convection
H_0	W·m^{-2}	Conductive heat flux density (heat flux by diffusion in a still fluid)
L	m	Height of the fluid layer (convection cell)
Nu	1	Nusselt number
Nu_c	1	Corrected Nusselt number
Nu_m	1	Measured Nusselt number
Pr	1	Prandtl number
Q_b	W	Heat power to the bottom plate
R	m	Radius of the plate
Ra	1	Rayleigh number
Ra_c	1	Critical Rayleigh number
Re	1	Reynolds number
S	m^2	Area of the plate
T_b	K	Temperature of the bottom plate
T_t	K	Temperature of the top plate
W	1	Wall number
ΔT	K	Vertical temperature difference
ΔT_{adiab}	K	Adiabatic temperature gradient
$\alpha\Delta T$	%	Boussinesq condition
α	K^{-1}	Isobaric thermal expansion coefficient
Γ	1	Aspect ratio
ν	m	Kinematic viscosity
κ	m^2s^{-1}	Thermal diffusivity
λ	$\text{W·m}^{-1}\text{·K}^{-1}$	Thermal conductivity of the fluid
λ_p	$\text{W·m}^{-1}\text{·K}^{-}$	Thermal conductivity of the plate
λ_w	$\text{W·m}^{-1}\text{·K}^{-1}$	Thermal conductivity of the sidewall
ρ	kg·m^{-3}	Density of He

11 Appendixes

Appendix 1: Results obtained by the SimRBC software for an experiment performed in the convection cell for a He density of 30 kg/m^3 and a Boussinesq condition $\alpha \cdot \Delta T = 0.2$.

Appendix 2: Helium control system

Appendix 3: Procedure of vacuum brazing

Appendix 1

Results obtained by the SimRBC software for an experiment performed in the convection cell for a He density of 30 kg/m^3 and a Boussinesq condition $\alpha \cdot \Delta T = 0.2$.

Density of He in the convection cell [kg/m^3]	30.0	30.0	30.0	30.0	30.0	30.0	30.0
Mean temperature [K]	4.800	5.000	5.200	5.400	5.600	5.800	6.000
Mean pressure [kPa]	166.6	180.5	194.5	208.5	222.5	236.5	250.6
Rayleigh number	4.49E+13	3.61E+13	3.02E+13	2.61E+13	2.30E+13	2.06E+13	1.87E+13
Boussinesq approximation $\alpha*\Delta T$ [%]	20.0	20.0	20.0	20.0	20.0	20.0	20.0
Prandtl number	2.2	1.89	1.69	1.55	1.44	1.37	1.31
Heat power to the bottom plate [W]	0.93	1.13	1.33	1.53	1.74	1.93	2.13
Temperature difference ΔT [mK]	164.0	206.8	249.7	292.7	335.9	379.1	422.4
Time of stabilization [h]	2.61	2.32	2.12	1.97	1.86	1.77	1.70
Consumption of LHe [Litre]	6.53	7.03	7.25	7.70	8.40	8.78	9.32
Density of He in the chamber [kg/m3]	9.00	7.00	5.50	4.70	4.30	3.80	3.50
Q_t [W]	0.07	0.08	0.03	0.03	0.07	0.04	0.05
$Q_t + Q_b$ [W]	1.00	1.21	1.37	1.56	1.80	1.98	2.19
Boundary layer thickness [mm]	0.073	0.078	0.083	0.087	0.090	0.093	0.096
Temperature of the upper plate [K]	4.718	4.897	5.075	5.254	5.432	5.610	5.789
Temperature of the bottom plate [K]	4.882	5.103	5.325	5.546	5.768	5.990	6.211

d(Nu^3/Ra)/d(quantity): increment							
$d\sigma$/dTrot 1mK	0.1979	0.1513	0.1223	0.1028	0.0886	0.0775	0.0682
$d\sigma$/dΔT 1mK	2.4387	1.9345	1.6021	1.3665	1.1910	1.0551	0.9469
$d\sigma$/dp 0.10%	-1.9781	-1.3287	-0.9720	-0.7841	-0.6391	-0.5834	-0.4834
d(Nu^3/Ra)/dQ 0.10%	0.3000	0.3000	0.3000	0.3000	0.3000	0.3000	0.3000

(Nu^3/Ra) errors of individual quantities:							
Error from Trot 3	0.594	0.454	0.367	0.308	0.266	0.232	0.205
Error from ΔT 2	4.877	3.869	3.204	2.733	2.382	2.110	1.894
Error from p 0.10	1.978	1.329	0.972	0.784	0.639	0.583	0.483
Error from Q_b 0.50	1.500	1.500	1.500	1.500	1.500	1.500	1.500

Maximal total uncertainty in Nu^3/Ra:	5.5	4.4	3.7	3.2	2.9	2.7	2.5

Ra+dRa	4.74E+13	3.76E+13	3.13E+13	2.69E+13	2.37E+13	2.12E+13	1.92E+13
Ra-dRa	4.24E+13	3.45E+13	2.91E+13	2.52E+13	2.23E+13	2.01E+13	1.83E+13

Appendix 2

Helium control system

Convection Cell

Label	Name	Description	Manufacturer
C-V1	Line B closing valve	AVC 016 PA, Angle valve, DN 16 ISO-KF	Pfeiffer Vacuum
C-V2	Connecting valve to the He recovery system	AVC 016 PA, Angle valve, DN 16 ISO-KF	Pfeiffer Vacuum
C-V3	Connecting valve for the pressure gauge C-PG1	Bellows valve Swagelok 1/4 VCR, type SS – 4H – V18	Swagelok
C-V4	Connecting valve to the rotary vacuum pump C+CH-RVP	AVC 016 PA, Angle valve, DN 16 ISO-KF	Pfeiffer Vacuum
C-SV1	Pressure safety valve on line A	Pressure safety valve (ISI) with bursting disc COMAT, absolute burst pressure 300 kPa , tol. 10%	ISI AS Brno, Comat, s.r.o.
C-SV2	Pressure safety valve on the line B	Pressure safety valve with spring, Model 595 AV, DN 3/4", pressure 1.7 bar	Armat, s.r.o.
C-PG1	Cell pressure gauge	Absolute Pressure Transducer Type 690A53TRB, range 5000 to 5 x 10 – 2 Torr, (658 kPa – 13 Pa), accuracy 0,08 % of Reading +/- Temp.Coeff., Fitting Swagelok Cajon 4VCR female, 1/4"	MKS Instruments, Inc.
C-PG2	Control pressure gauge for the cell	BD – Sensor, DMP 331i, absolute, pressure range 0 – 4 bar, accuracy 0.1% FSO IEC 60770, mech. connection M 20 x 1.5 DIN 3852	BD Sensors
C-VG1	Vacuum gauge	DI 200, range 1 – 200 mbar, membrane vacuum gauge	Leybold Vakuum
C+CH-RVP	Rotary vane vacuum pump	Edwards RV8, final pressure 1E-1 Pa	Edwards

Heat Exchange Chamber

Label	Name	Description	Manufacturer
CH-V1	Closing valve of line C	AVC 016 PA, Angle valve, DN 16 ISO-KF	Swagelok, Pfeiffer
CH-V2	Connecting valve to the recovery system	AVC 016 PA, Angle valve, DN 16 ISO-KF	Pfeiffer Vacuum
CH-V3	Connecting valve to the vacuum pump	AVC 016 PA, Angle valve, DN 16 ISO-KF	Pfeiffer Vacuum
CH-SV1	Pressure safety valve on line C	Pressure safety valve with spring, pressure 150 kPa (abs.)	ISI AS Brno
CH-VG1	Vacuum gauge	Active Capacitance Transmitter CMR 363, pressure range 0 – 1.6 bar, accuracy 0.05% FSO, DN 16 ISO-KF	Pfeiffer Vacuum
CH-VG2	Vacuum gauge	DI 200, range 1 – 200 mbar, membrane vacuum gauge	Leybold Vakuum
C+CH-RVP	Rotary vane vacuum pump	Edwards RV8, final pressure 1E-1 Pa	Edwards

LHe Vessel

Label	Name	Description	Manufacturer
HeV-V1	Connecting valve to the recovery system		ISI AS Brno
HeV-SV1	Pressure safety valve on line D	Pressure safety valve with spring, pressure 1.1 bar	ISI AS Brno
HeV-SV2	Pressure safety valve on line D	Pressure safety valve with spring, pressure 1.5 bar	ISI AS Brno

Outer Shell

Label	Name	Description	Manufacturer
OS-SV1	Safety valve		ISI Brno
OS-V1	Connecting valve to the vacuum pump system	UHV valve, bellows sealed	ISI Brno
OS-VG1	Vacuum gauge	Ionisation vacuum gauge IV1, pressure range 1E-2 – 1E-7 Pa	Laboratorní přístroje Praha
OS-RVP and OS-TMP	Vacuum pump station	TurboCube TSH 071, Turbomolecular pump with rotary vane pump, DN 40 ISO-KF, final pressure < 1E-5 Pa	Pfeiffer Vacuum

Appendix 3

Procedure of vacuum brazing

Preparation

Washing	SimpleGreen 1:4
Rinse	water
Masking	cement Nicrobraz 310

Elektrolytic etching

H2SO4	200 g/litre
Current	$0.1 A/cm^2$ (17.5 A)
Temperature	room temperature
Sample as cathode	10 s
Sample as anode	15 s
Will be ate away	from 0.2 to 0.3 μm

Nickel plating in Woods nickel strike

NiCl2	250 g/litre
HCl	200 g/litre
Nickeling piece on cathode, anode Ni	
Current	$0.2 A/cm^2$
Temperature	room temperature
Ni layer increase	1 μm per 4 minutes
Time of nickel plating	6 minutes

Removal of masking

Remove Nicrobraz 310, possibly wipe away

Vacuum brazing of the Cu plate and the stainless steel ring

Brazing solder	Cu28Ag72
Start-up	760°C
Time of brazing	1 hour
Raise on	780°C
Rapid raise of temperature	up to 840°C